Supralinear dendritic integration in murine dendrite-targeting interneurons

Authors and affiliations

Simonas Griesius[1], Dimitri M Kullmann[1]*

[1]Department of Clinical Experimental and Epilepsy, UCL Queen Square Institute of Neurology,

University College London, London, WC1N 3BG, United Kingdom

*Corresponding author and lead contact

Correspondence: d.kullmann@ucl.ac.uk

Running title: Supralinear dendritic integration in interneurons

Keywords: Calcium imaging, nonlinear summation, synaptic plasticity, L-type calcium channel, credit assignment, neurogliaform, oriens-lacunosum moleculare, OLM, plateau potential, SERCA

Acknowledgements

We thank all members of the Kullmann lab and the wider Department of Clinical and Experimental Epilepsy for contributing to discussions surrounding the presented work. We thank Dr Amy Richardson for the development of the virus used to drive reporter expression.

Funding: The authors gratefully acknowledge support from the Wellcome Trust (212285/Z/18/Z).

Conflict of interest: The authors declare no conflicts of interest.

Author contributions: Conceptualization, S.G and D.M.K; Methodology, S.G and D.M.K; Software, S.G; Validation, S.G and D.M.K; Formal Analysis, S.G and D.M.K; Investigation, S.G; Resources, D.M.K; Data Curation, S.G; Writing – Original Draft, S.G and D.M.K; Writing

– Review & Editing, S.G and D.M.K; Visualization, S.G and D.M.K; Supervision, D.M.K; Project Administration, S.G and D.M.K; Funding Acquisition, D.M.K;

Abstract

Non-linear summation of synaptic inputs to the dendrites of pyramidal neurons has been proposed to increase the computation capacity of neurons through coincidence detection, signal amplification, and additional logic operations such as XOR. Supralinear dendritic integration has been documented extensively in principal neurons, mediated by several voltage-dependent conductances. It has also been reported in parvalbumin-positive hippocampal basket cells, in dendrites innervated by feedback excitatory synapses. Whether other interneurons, which support feed-forward or feedback inhibition of principal neuron dendrites, also exhibit local non-linear integration of synaptic excitation is not known. Here we use patch-clamp electrophysiology, and 2-photon calcium imaging and glutamate uncaging, to show that supralinear dendritic integration of near-synchronous spatially clustered glutamate-receptor mediated depolarization occurs in NDNF-positive neurogliaform cells and oriens-lacunosum moleculare interneurons in the mouse hippocampus. Supralinear summation was detected via recordings of somatic depolarizations elicited by uncaging of glutamate on dendritic fragments, and, in neurogliaform cells, by concurrent imaging of dendritic calcium transients. Supralinearity was abolished by blocking NMDA receptors (NMDARs) but resisted blockade of voltage-gated sodium channels. Blocking L-type calcium channels abolished supralinear calcium signalling but only had a minor effect on voltage supralinearity. Dendritic boosting of spatially clustered synaptic signals argues for previously unappreciated computational complexity in dendrite-projecting inhibitory cells of the hippocampus.

Introduction

Accumulating evidence indicates that dendrites do more than merely summate excitatory and inhibitory synaptic inputs[1-6]. Dendrites endow neurons with increased computational capacity[7] and the ability to act as multi-level hierarchical networks[8,9] or even to reproduce some features of artificial and deep neural networks[10,11]. The underlying mechanisms include extensive dendritic arborisation, compartmentalisation, synaptic plasticity and expression of specific receptors and ion channels that in turn facilitate nonlinear input summation. Nonlinear dendritic integration of excitatory inputs in particular can potentially support signal amplification[12], coincidence detection[13], XOR logic gating[14,15], and computing prediction errors[2,11]. One striking example of non-linear integration is local supralinear summation of signals that arrive at a dendritic fragment in a narrow time window, a phenomenon that can

be investigated by exploiting the spatial and temporal precision of somatic depolarizations elicited by multi-photon glutamate uncaging[16-21]. Several receptors and channels have been implicated in supralinear summation in principal neurons, including NMDARs[16-19,21-27], calcium-permeable AMPARs[21,25,26], and voltage-gated sodium channels[20,21,24,25,27,28], calcium channels[19,21,25,27], and potassium channels[29,30]. Closely related to voltage supralinearity is the occurrence of dendritic calcium transients which can be detected with calcium-sensitive fluorescent indicators. Such calcium transients are implicated in synaptic plasticity and result not only from influx via voltage-dependent channels but also release from intracellular stores[25,26,31,32].

Inhibitory interneurons have a crucial role in brain circuit and network excitability, rhythmicity, and computations[33-35]. However, in comparison with principal cells, relatively little is known about non-linear dendritic integration in interneurons. Early evidence for NMDAR-dependent supralinear summation of EPSPs, and dendritic calcium transients, in hippocampal CA1 interneurons was not accompanied by molecular or genetic markers of interneuron type[18]. Subsequent studies in parvalbumin-positive (PV+) interneurons reported supralinearly summating EPSPs and dendritic calcium transients[21,25,26]. Using multiphoton glutamate uncaging for increased spatial precision, Cornford et al. also showed evidence for NMDAR-dependent supralinear EPSP summation in PV+ basket cells, although this was only seen in dendrites receiving feedback excitation in stratum oriens and not in dendrites receiving feed-forward excitation in stratum radiatum[16]. Failure to detect supralinear summation in stratum radiatum dendrites of PV+ interneurons is consistent with evidence from dendritic recordings that somatic action potentials attenuate rapidly as they back-propagate, and that PV+ dendrites express abundant Kv3 family potassium channels and relatively few sodium channels[36]. Indeed, compartmental modelling has been used to infer that synaptic inputs to PV+ interneuron dendrites summate sublinearly, and that this helps to ensure that they do not disrupt population spike synchrony during gamma oscillations[37]. In contrast to the evidence for both supra- and sublinear summation in PV+ interneurons (likely to occur simultaneously in different dendrites)[16], it remains unknown how synaptic inputs are integrated in other forebrain interneurons. As for other brain regions, cerebellar cortex stellate cells have been shown to exhibit sublinear summation of uncaging-evoked EPSPs whilst simultaneously exhibiting supralinear summation of dendritic calcium transients[19].

Dysfunction of interneurons generally has been associated with a variety of psychiatric and neurological pathologies, including epilepsy[38-41], schizophrenia [42-44], autism spectrum disorder[44,45] and Alzheimer's diease[46,47], among others[48]. There is emerging evidence suggesting that impairments in dendritic integration[20,49-52], and specifically in interneurons[20], may be important contributors to pathological phenotypes in psychiatric and neurological

pathologies. We therefore set out to characterize dendritic integration in two types of interneurons innervating the distal dendrites of CA1 pyramidal neurons: PV-negative neurogliaform interneurons, which support feed-forward inhibition, and oriens-lacunosum moleculare (OLM) cells, which additionally mediate feedback inhibition. Although their cell bodies reside in different layers, and their developmental origin and intrinsic properties are strikingly different[48,53-58], their axons innervate the same targets, the apical tuft dendrites of pyramidal neurons in the SLM. Neurogliaform cells receive inputs from the entorhinal cortex and the nucleus reuniens[56], with distinct plasticity rules at synapses made by these afferents[59], and a subset can be identified in stratum lacunosum-moleculare (SLM) using knock-in mice expressing cre recombinase at the neuron-derived neurotrophic factor (NDNF) locus[56,58-60]. OLM cells, in contrast, have their cell bodies and dendrites in stratum oriens, are excited by axon collaterals of both CA1 and CA3 pyramidal neurons, and can be identified using mice expressing cre at the somatostatin locus [61].

We quantified non-linear dendritic summation using 2-photon glutamate uncaging at multiple locations within a small dendritic fragment, by comparing the arithmetic sum of the uncaging-evoked EPSPs evoked individually to the result of near-synchronous glutamate uncaging[16]. We asked if neurogliaform and OLM interneurons exhibit non-linear summation and whether this depends on NMDARs or sodium or calcium channels. In parallel, we asked if non-linear summation could also be detected in these cell types by concurrent measurement of dendritic calcium-dependent fluorescence transients.

Results

Supralinear dendritic integration in a representative neurogliaform interneuron

NDNF-positive (NDNF+) neurogliaform interneurons were studied in the hippocampal CA1 stratum lacunosum/moleculare in acute slices from NDNF-cre mice injected with AAV2/9-mDLX-FLEX-mCherry virus (Fig. 1a). In order to probe the spatiotemporal dynamics of dendritic integration, glutamate was locally delivered by 2-photon uncaging of bath-perfused MNI-glutamate (3 mM) using an infrared (720nm) pulsed laser at points along dendrites, whilst recording from their somata with a patch pipette. The absence of dendritic spines prevented identification of the sites of excitatory synapses, and the uncaging locations were therefore spaced 1 – 2 µm apart, either side of the selected dendritic fragment[16] (Fig. 1b). The locations were kept within a dendritic length of ~15 µm, consistent with the size of interneuron dendritic domains exhibiting correlated tuning of synaptic calcium transients in vivo[62]. Glutamate uncaging was achieved with 0.5 ms pulses separated by an interval of either 100.32 ms (asynchronously) or 0.32 ms, near-synchronously. The number of uncaging stimuli at neighbouring locations was cumulatively increased from 1 to 12 in the near-synchronous condition (Fig. 1c). In the illustrated example, the somatic uEPSP evoked by near-synchronous uncaging was substantially greater in amplitude and duration than predicted from the arithmetic sum of the individual somatic uEPSPs (Fig. 1d).

In parallel with measurement of uEPSPs, we measured dendritic calcium transients by monitoring the fluorescence of the calcium sensor Fluo-4, which was included in the pipette solution, using a second pulsed infrared scanning laser tuned to 810 nm (Fig 1e, f). The interval between glutamate uncaging pulses in the asynchronous condition was too short to allow the dendritic Fluo-4 signal to relax to baseline in between stimuli. Instead, we examined the peak amplitude of the dendritic calcium response, either in response to asynchronous uncaging at all 12 locations (Fig. 1e) or with an increasing number of near-synchronous stimuli (Fig. 1f). This revealed a discontinuity, where the amplitude of the dendritic calcium fluorescence transient increased abruptly with 6 or more near-synchronous uncaging locations, and exceeded the fluorescence observed with asynchronous uncaging at all 12 locations (Fig. 1e, f).

In order to characterize non-linear voltage integration measured at the soma, the amplitude of the observed uEPSP elicited by near-synchronous uncaging at an increasing number of locations was plotted against the arithmetic sum of the individual responses. Consistent with supralinear integration in principal neurons and at oriens dendrites in PV+ interneurons, as the number of uncaging sites was increased, the recorded near-synchronously evoked uEPSPs initially summated approximately linearly, and then deviated from the line of identity

upon activation of multiple uncaging locations (Fig. 1g). The supralinearity was more marked when the uEPSP was quantified by integrating the somatic depolarization for 100ms (Fig. 1h), as expected from the recruitment of voltage-dependent conductances. As the number of uncaging locations was increased further, the peak amplitude and integral showed a tendency to reach a plateau, consistent with a decrease in driving force as the local dendritic membrane potential approached the synaptic reversal potential.

To estimate the supralinearity of the calcium transients, we interpolated the calcium response from 1 location uncaged to the maximal fluorescence observed with all 12 locations uncaged asynchronously, and compared the peak amplitude of the calcium transients as an increasing number of locations were uncaged near-synchronously (Fig. 1i). This revealed an abrupt deviation from the interpolated line at 6 locations uncaged, with a further increase as more locations were uncaged, before the observed response reached a plateau.

Supralinear dendritic integration in neurogliaform interneurons

We examined dendritic nonlinearity in a sample of neurogliaform NDNF+ interneurons studied in the same way. This revealed robust supralinear integration of uEPSP amplitude (Fig. 2a). The overall shape of the relationship between the observed and expected amplitude varied among cells, although its sigmoid shape persisted. We took as a measure of supralinearity in each cell the cumulative relative deviation of the observed amplitude from the expected value (see Methods). Including cells that were used for subsequent blockade of NMDARs (see below), the overall average amplitude supralinearity was 58 ± 20% (average ± SEM, n = 11, deviation from 0, P<0.001; Fig. 2b). Consistent with the data from the sample neuron (Fig. 1) the degree of voltage nonlinearity was more marked for the voltage integral measured over 100 ms (integral nonlinearity 122 ± 35%), implying the involvement of slow and/or regenerating conductances (Fig. 2c, d). As for dendritic calcium transients, 6 out of 7 interneurons where they were measured exhibited a greater than predicted Fluo-4 fluorescence transient, with a nonlinearity estimated at 37 ± 10% (P=0.0138; Fig. 2e, f).

Previous studies on dendritic integration have generally examined either voltage or dendritic calcium signalling in isolation, with the exception of an investigation of cerebellar layer molecular interneurons, which reported a striking dissociation, where calcium signalling exhibited supralinear summation while voltage summation was sublinear[19], contrasting with the present results. The present findings suggest that dendritic regenerative currents are calcium-permeable, and that the calcium supralinearity is causally downstream from the voltage supralinearity. This principle was supported by the similar sigmoid shapes of the observed near-synchronous uEPSP amplitudes and calcium transients in the cell illustrated

in Fig. 1. Some cells exhibited a prominent plateau potential upon near-synchronous uncaging, with a peak calcium transient proportional to the uEPSP integral (Pearsons' correlation coefficient r = 0.95; Fig. S1). However, across the sample of 7 cells, the correlation coefficient relating calcium to voltage supralinearity varied substantially and was not systematically greater for voltage integral (0.44 ± 0.16, average ± SEM) than for peak uEPSP amplitude (0.47±0.18).

Among possible sources of variability for voltage supralinearity, we did not observe a systematic dependence on the average amplitude of individual uEPSPs, distance from the uncaging location along the dendrite to the soma, or the dendrite order (Fig. S2).

Sublinear dendritic integration in neurogliaform interneurons with NMDARs blocked

Several conductances have been implicated in supralinear integration in principal neuron dendrites, including NMDARs[16-19,21-27], sodium channels[20,21,24,25,27,28] and calcium channels[19,21,25,27]. We asked whether they have similar roles in neurogliaform cells.

In a subset of cells reported in Fig. 2, we applied the NMDAR antagonist D-AP5 by bath perfusion. This robustly abolished voltage supralinearity, whether measured as the peak amplitude of uEPSPs ($P<0.001$, n = 6; Fig. 3a, c, d) or uEPSP integral ($P<0.001$; Fig. 3e, f). Summation of somatic uEPSPs became sublinear ($P<0.001$, $P<0.001$, for peak and integral respectively), consistent with the behaviour of a passive dendrite where the local synaptic driving force and impedance diminish as an increasing number of glutamate receptors open. Dendritic calcium fluorescence transients were also profoundly reduced (Fig 3b, g, h).

Supralinear dendritic integration in neurogliaform interneurons does not require voltage-dependent sodium channels

We examined the role of voltage-gated sodium channels, which have been implicated in back-propagating action potentials in principal cells[63-65], by repeating the study in the continuous presence of tetrodotoxin (TTX). In a representative cell, robust supralinear integration was seen for both uEPSPs (Fig. 4a) and calcium fluorescence transients (Fig. 4b). Across all dendrites tested (n = 7), both the uEPSP and the dendritic calcium transient amplitudes summated supralinearity (Fig. 4c-h), with effect sizes closely resembling those observed in the drug-free condition (Fig. 2). The data argue against a contribution of voltage-gated sodium channels to supralinear dendritic integration in NDNF+ neurogliaform interneurons.

L-type voltage-dependent calcium channel blockade abolishes nonlinear dendritic calcium summation

In another group of neurogliaform cells, we examined dendritic integration in the presence of the L-type voltage-dependent calcium channel blocker nimodipine. Although the population average non-linearity was not different from 0, a subset of neurons continued to show supralinear summation for both peak and integral (Fig. 5a, c-f), contrasting with the effect of blocking NMDARs. Dendritic calcium transients were profoundly attenuated (Fig. 5b, g, h). We tentatively conclude that L-type calcium channels have a smaller contribution to voltage supralinearity than NMDARs, but contribute substantially to dendritic calcium influx.

SERCA inhibition abolishes nonlinear dendritic calcium summation

We next asked if release from intracellular stores also contributes to dendritic calcium transients, as has been reported in stratum oriens interneurons[26]. We therefore examined the effect of depleting calcium stores with the SERCA inhibitor cyclopiazonic acid (CPA). Although voltage supralinearity persisted (Fig. 6a, c-f), dendritic calcium transients were abolished (Fig. 6b, g, h).

A parsimonious explanation for the dissociation of voltage supralinearity and calcium signalling is that NMDARs are the main driver of regenerative currents in the dendrites of neurogliaform cells, and that calcium influx via NMDARs and L-type calcium channels is amplified by calcium release from intracellular stores. Overall, the robust NMDAR-mediated supralinearity demonstrated in neurogliaform cells stands in contrast to the more subtle supralinearity observed in PV+ interneurons in response to an identical glutamate uncaging protocol, which was confined to dendrites in stratum oriens[16].

Supralinear dendritic integration in OLM interneurons

Apical tuft dendrites of pyramidal neurons are innervated not only by neurogliaform cells but also by OLM interneurons, which exhibit numerous differences with respect to their developmental origin, morphology and intrinsic and synaptic properties. We asked whether the robust supralinear summation and calcium signalling exhibited by neurogliaform cells are also a feature of OLM cells, by repeating the experiments using multiphoton uncaging on dendrites in stratum oriens. OLM cells were identified in acute hippocampal slices from SOM-Cre x Ai9 mice, with dendrites running parallel to stratum pyramidale and an axon, where visualised, extending through stratum pyramidale and stratum radiatum (Fig 7a, b).

Uncaging-evoked uEPSPs summated supralinearly in OLM cells, as detected by comparing either the peak amplitude or voltage integral of near-synchronously evoked responses to the arithmetic sum of the asynchronously evoked responses (Fig. 7c-g).

Linear dendritic integration in neurogliaform interneurons with NMDARs blocked

As for neurogliaform cells, there was no obvious dependence of the magnitude of supralinearity on the average size of the individual uEPSPs, dendritic distance or dendrite order (Fig. S3). NMDAR blockade abolished supralinearity (Fig. 8a-e), further underlining the similarity with neurogliaform cells. However, sublinear summation was not observed in D-AP5. Another striking difference was that the uEPSPs evoked in OLM cells (with NMDARs intact) were sub-threshold for detectable dendritic calcium signals.

No effect of voltage-dependent sodium channel nor of L-type voltage-dependent calcium channel blockade

Neither sodium channel blockade (Fig. 8f-j), nor calcium channel blockade (Fig. 8k-o) prevented supralinear summation of uEPSPs. Depletion of intracellular calcium stores with CPA also had no effect (Fig. S4). The magnitude of supralinearity in the presence of either TTX or nimodipine was no different from the magnitude in the absence of blockers. The data thus point to a model where supralinearity is mediated exclusively by NMDARs, and occurs with uEPSPs that are subthreshold for dendritic calcium signalling.

The absence of sublinear summation in D-AP5 is reminiscent of the pattern observed in stratum oriens dendrites of PV+ interneurons[16], as is the relative magnitude of supralinearity. When neurogliaform and OLM data obtained in TTX were grouped together with the data without blockers, the supralinearity for voltage integral in OLM interneurons was significantly smaller than that in neurogliaform cells (Fig. 8p). A possible explanation is that the local dendritic impedance is greater in neurogliaform cells, lowering the threshold for recruitment of regenerative currents. Consistent with such a pattern, the local dendrite diameter of neurogliaform interneurons was significantly lower than that of OLM cells (Fig. 8q). A morphological difference may thus contribute to the smaller voltage and calcium supralinearities in OLM than neurogliaform cells.

Discussion

The main results of the present study are that both hippocampal neurogliaform interneurons and OLM cells exhibit robust NMDAR-dependent supralinear integration of dendritic uEPSPs recorded at the soma. Supralinear NMDAR-dependent integration was also observed by measuring dendritic calcium fluorescence transients in neurogliaform cells, which were sensitive to blockade of L-type calcium channels or depletion of intracellular stores. However, near-synchronous glutamate uncaging that was sufficient to elicit NMDAR-dependent boosting of uEPSPs failed to recruit detectable dendritic calcium transients in OLM cells. In contrast to principal neurons, we observed no role for voltage-gated sodium channels in dendritic integration of uEPSPs in either cell type.

Taken together, the data are consistent with a model where clustered synaptic receptor activation leads to relief of voltage-dependent block of dendritic NMDARs by magnesium ions, accounting for supralinear summation of uEPSPs recorded at the soma. In neurogliaform cells (although apparently not in OLM cells) L-type voltage-gated calcium channels are also recruited by the local depolarization, and together with calcium influx via NMDARs, the resulting local elevation of intracellular calcium triggers further release from intracellular stores, thereby amplifying the dendritic calcium concentration transient. This account of the signalling cascade underlying local calcium signalling does not exclude additional roles for metabotropic glutamate receptors and calcium influx via rectifying calcium-permeable glutamate receptors, which have been implicated in dendritic calcium transients in oriens interneurons[26].

The dependence of supralinear dendritic summation on NMDARs but not voltage-gated sodium channels is reminiscent to the pattern observed at dendrites of parvalbumin-positive interneurons in stratum oriens[16]. NMDARs have previously been implicated in synaptic signalling in neurogliaform cells[56,57,66] and also contribute to long-term potentiation[59]. Indeed, the ratio of NMDAR- to AMPAR-mediated signalling at glutamatergic synapses on neurogliaform cells has been shown to be higher than in other hippocampal interneuron subtypes[56]. This feature may explain why NMDAR-mediated supralinear integration is especially prominent in neurogliaform cells, although a further contribution may come from their unusually thin and short dendrites, which would be expected to represent a high impedance, thus facilitating their depolarization by glutamate receptor activation.

OLM cells exhibited several differences in comparison with neurogliaform cells. First, supralinear voltage integration was smaller. Second, blockade of NMDARs led to linear, as opposed to sublinear summation of uEPSPs. And third, uEPSPs evoked by glutamate uncaging, whether asynchronous or near-synchronous, were subthreshold for robust

dendritic calcium transients. These differences can be explained by a relatively lower expression of NMDARs and/or lower dendritic impedance as expected from larger dendritic diameter and length. Indeed, we confirmed that the dendritic diameter at the uncaging locations was larger in OLM than neurogliaform cells. A further morphological difference is that the dendrites of OLM cells are equipped with sparse thin spines[67,68], although we did not visuallize them.

The present study highlights the ability of both neurogliaform and OLM neurons to perform local computations upstream of the site of axonal action potential initiation. The adaptive significance of this phenomenon remains to be determined. In principal neurons, synaptic inputs converging to common dendritic domains have been shown to exhibit correlated activity[69-71]. Synaptically evoked calcium transients in dendritic domains of interneurons of the visual cortex have also been reported to exhibit orientation tuning that is not apparent in the global activity recorded at the soma[62]. The dendritic nonlinearities uncovered by the present study, together with different forms of synaptic plasticity described in interneurons[72], are a candidate mechanism to achieve such an organization of information processing.

Material and methods

Animal and husbandry

Adult male and female mice of varying ages were throughout the study (ages 1-3 months). Transgenic mouse lines were maintained as heterozygotes. NDNF-cre+/+ or NDNF-cre+/- mice (The Jackson Laboratory B6.Cg-Ndnftm1.1(folA/cre)Hze/J; Stock No: 028536; Bar Harbor, ME, USA), bred on a C57BL/6 background) were used to target neurogliaform interneurons[73]. SOM-cre+/+ (The Jackson Laboratory Ssttm2.1(cre)Zjh/J; Stock No: 013044; Bar Harbor, ME, USA) crossed with Ai9+/+ mice (The Jackson Laboratory B6.Cg-Gt(ROSA)26Sortm9(CAG-tdTomato)Hze/J; Stock No: 007909; Bar Harbor, ME, USA) were used to target OLM interneurons[61,74]. Animals were group-housed under a normal 12 h light/dark cycle. Cages were enriched with paper bedding, cardboard tube, plastic tube, and wooden chewing blocks. Mice had had unlimited access to standard laboratory chow and water. All procedures were carried out in accordance with the UK Animals (Scientific Procedures) Act, 1986.

Surgery for viral injection

Mice of at least 6 weeks of age were anaesthetised with isoflurane and placed into a stereotaxic frame, onto a heating pad to maintain body temperature. Mice were given Metacam (0.1 mg/kg) and buprenorphine (0.02 mg/kg) subcutaneously. Bilateral craniotomies were performed, positioned 3.1 mm caudal and ±3.12 mm lateral of Bregma. Virus (AAV2/9-mDlx-FLEX-mCherry; titre >10^{12} viral genomes/ml; VectorBuilder (Chicago, IL, USA)) was injected into the ventral CA1 region of both hippocampi using a Hamilton syringe 2.5 mm deep from the pia. 150 nL of virus was injected at each site at a rate of 100 nL/min. The needle was left in place for 5 min following injections before withdrawal. Mice were given 0.5 mL saline subcutaneously post-operatively to help with recovery and were monitored for 5 days following the procedure. Mice were sacrificed for experiments after a minimum of 3 weeks post-surgery.

Brain Slice preparation

Mice were sacrificed, the brains removed, and hippocampi dissected and sliced in ice-cold sucrose-based solution containing (in mM): 205 Sucrose, 10 Glucose, 26 NaHCO3, 2.5 KCl, 1.25 NaH2PO4, 0.5 CaCl2, 5 MgSO4, saturated with 95% O2 and 5% CO2. Transverse 400 µm hippocampal slices were cut using a Leica VT1200S vibrating microtome. Slices were incubated in artificial cerebrospinal fluid (aCSF) at 35 °C for 30 min and then at room temperature for 30 min. aCSF contained (in mM): mM: 124 NaCl, 3 KCl, 24 NaHCO3, 1.25 NaH2PO4 10 Glucose, 2.5 CaCl2, 1.3 MgSO4, saturated with 95% O2 and 5% CO2. The

CA3 area was removed prior to slice transfer into the recording chamber to prevent recurrent activity.

Electrophysiology

The recording chamber was perfused with oxygenated aCSF maintained at 32 °C. Slices were first visualised using Dodt illumination on an Olympus FV1000 BX61 microscope. Fluorescent cells were identified either in the CA1 stratum lacunosum/moleculare (neurogliaform cells) or the stratum oriens (OLM cells) using Xcite epifluorescence. Borosilicate glass pipettes (pipette resistance of 4-5 MΩ) were pulled using a horizontal P2000 Sutter-instruments puller. The internal solution contained (in mM) 120 KMeSO3, 8 NaCl, 10 HEPES, 4 Mg-ATP, 0.3 Na-GTP, 10 KCl, ~295 mOsm, 7.4 pH. EGTA was not added to avoid introducing excess calcium buffering capacity. Internal solution aliquots were filtered on the day of experiment and small volumes of Alexa Fluor-594 (final concentration 50 μM) and Fluo-4 (final concentration 400 μM) solution aliquots were added. Recordings were obtained using a Multiclamp 700B Molecular Devices (USA) amplifier filtered at 10 kHz and digitized at 20 kHz (National Instruments PCI-6221, USA). WinWCP 5.5.6 (John Dempster, University of Strathclyde) software was used for data acquisition. After whole-cell break-in in V-clamp, the cells were switched to I=0 mode briefly to measure the resting membrane potential, before switching to I-clamp mode for experiments. All experiments were performed in I-clamp mode, with current continuously injected to maintain cell membrane between at ~−65 mV (0 to -50 pA). All data are presented without adjustment for the junction potential (~−15 mV). Recordings were discarded if they had an access resistance >25 MΩ and if access or input resistance changed by >20% over the course of the experiment. All experiments were conducted in the presence of picrotoxin 50 μM and CGP55845 1 μM to block GABAergic transmission. D-AP5 (50 μM), tetrodotoxin (TTX) (200 nM), nimodipine (30 μM), cyclopiazonic acid (CPA) (30 μM) were bath-applied to block NMDARs, voltage-activated sodium channels, L-type calcium channels, or to inhibit SERCA respectively. D-AP5 was applied over a period of 7 minutes following a control recording, whilst TTX, nimodipine, and CPA were present in the recording chamber throughout their respective experiments.

Two-photon imaging and uncaging

Simultaneous two-photon imaging and uncaging of MNI-caged glutamate were performed using two Ti-sapphire lasers tuned to 810 nm and 720 nm, for imaging and uncaging respectively (Mai-Tai, Spectra Physics, USA; Chameleon, Coherent, USA). MNI-caged-glutamate (3 mM; Hello Bio, UK) was added to the aCSF in a closed recirculating system upon patch-clamp break-in. 12 uncaging locations ~2 μm apart and <1 μm away from the

dendrite were chosen on either side of dendrites in pseudo-random patterns. 0.5 ms-long pulses of 720 nm light were used to uncage MNI-caged-glutamate. The uncaging light pulses were separated by either 100.32 ms or 0.32 ms in the control asynchronous (separate responses) or the near-synchronous protocols respectively. In the near-synchronous protocol, increasing numbers of uncaging locations were activated in a cumulative manner across sweeps 1 to 12. Inter-sweep interval was >30 s, during which adjustments were made to account for any focal and x-y drift. Cycles of control asynchronous and near-synchronous stimulation protocols were done one after the other to produce mean responses, without changing the order of dendritic locations uncaged. Uncaging times and locations were controlled by scanning software (Fluoview 1000V) and a pulse generator (Berkeley Nucleonics, Ca, USA) with a Pockels cell. Calcium signals were acquired using 810 nM laser light, linescanning on the same dendritic branch as the uncaging and down-stream of the uncaging locations toward the soma. Cells were discarded upon observation of photodamage or upon change in resting membrane potential of >10 mV. All z-stacks used for the analysis of morphology and example figures were captured at the end of experiments to maximise the amount of time for experiments before cell health deterioration. Photomultiplier tube filters used: 515–560 nm (Fluo-4); 590–650 nm (Alexa-594).

Quantification and statistical analyses

Amplitude and integral nonlinearity were regarded as the primary experimental outcomes.

Response nonlinearity was quantified using the following equation[16,75].

$$\%\,nonlinearity = \sum_{i=2}^{n} \frac{\frac{Mi}{Ai} - 1}{n-1} * 100\%$$

Mi amplitude of the ith measured uEPSP (composed of i individual uncaging spots)

Ai amplitude of the ith constructed arithmetically summed uEPSP

n is the total number of uncaging locations.

Seeing as the calcium signal did not return to its pre-stimulation baseline in between flashes of uncaging laser light in the control asynchronous (separate responses) condition, calculating the arithmetic sum of individual responses was not possible. Therefore, to obtain an estimate of nonlinearity for calcium traces, values from linear interpolation were used. The first sweep of the test condition, where only a single location was stimulated using

uncaging light, was treated as the first value of the control asynchronous (separate responses) condition for the purposes of interpolation. The second and final value used for interpolation was from the end of the control (separate responses) trace, so that the signal would encompass all 12 uncaging events.

Calcium signals were quantified using the following equation:

$$\Delta F / A$$

ΔF relative change in the Fluo-4 green channel fluorescence from baseline

A Alexa-594 red channel fluorescence

Traces including action potentials were excluded from analysis. Asynchronous separate uEPSPs were staggered by 0.82 ms for arithmetic summation to replicate the near-synchronous uncaging condition. Voltage and calcium traces were filtered using a Savitzky-Golay filter. Uncaging light artefacts were removed from linescans. Due to the substantial variability in responses across dendrites, dendrites were used as the experimental unit. The numbers of dendrites, cells, and animals are reported in figure legends. $\alpha = 0.05$ was applied for all statistical tests. The degrees of freedom, t, and p values are presented in the figure legends and discussed in text, as appropriate. Estimation statistics[76] and the generation of slopegraphs and Gardner-Altman estimation plots were performed using code provided by Ho et al.[77]. 95% confidence intervals of the mean difference were calculated by bootstrap resampling with 5000 resamples. The confidence interval is bias-corrected and accelerated. P values are provided with estimation statistics for legacy purposes only. Data were processed using custom Python code[78,79], Microsoft Excel, and WinWCP 5.5.6 (John Dempster, University of Strathclyde). Figures were created using custom Python code, Microsoft PowerPoint, Procreate, ImageJ.

References

1. Makarov, R., Pagkalos, M., and Poirazi, P. (2023). Dendrites and efficiency: Optimizing performance and resource utilization. Curr Opin Neurobiol *83*, 102812. 10.1016/j.conb.2023.102812.
2. Mikulasch, F.A., Rudelt, L., Wibral, M., and Priesemann, V. (2023). Where is the error? Hierarchical predictive coding through dendritic error computation. Trends Neurosci *46*, 45-59. 10.1016/j.tins.2022.09.007.
3. Poirazi, P., and Papoutsi, A. (2020). Illuminating dendritic function with computational models. Nat Rev Neurosci *21*, 303-321. 10.1038/s41583-020-0301-7.
4. Larkum, M.E., Wu, J., Duverdin, S.A., and Gidon, A. (2022). The Guide to Dendritic Spikes of the Mammalian Cortex In Vitro and In Vivo. Neuroscience *489*, 15-33. 10.1016/j.neuroscience.2022.02.009.
5. Stuart, G.J., and Spruston, N. (2015). Dendritic integration: 60 years of progress. Nat Neurosci *18*, 1713-1721. 10.1038/nn.4157.
6. Tran-Van-Minh, A., Caze, R.D., Abrahamsson, T., Cathala, L., Gutkin, B.S., and DiGregorio, D.A. (2015). Contribution of sublinear and supralinear dendritic integration to neuronal computations. Front Cell Neurosci *9*, 67. 10.3389/fncel.2015.00067.
7. Lorenzo, J., Binczak, S., and Jacquir, S. (2022). A multilayer-multiplexer network processing scheme based on the dendritic integration in a single neuron. AIMS Neurosci *9*, 76-113. 10.3934/Neuroscience.2022006.
8. Kim, Y.J., Ujfalussy, B.B., and Lengyel, M. (2023). Parallel functional architectures within a single dendritic tree. Cell Rep *42*, 112386. 10.1016/j.celrep.2023.112386.
9. Ujfalussy, B.B., Makara, J.K., Lengyel, M., and Branco, T. (2018). Global and Multiplexed Dendritic Computations under In Vivo-like Conditions. Neuron *100*, 579-592 e575. 10.1016/j.neuron.2018.08.032.
10. Beniaguev, D., Segev, I., and London, M. (2021). Single cortical neurons as deep artificial neural networks. Neuron *109*, 2727-2739 e2723. 10.1016/j.neuron.2021.07.002.
11. Wybo, W.A.M., Tsai, M.C., Tran, V.A.K., Illing, B., Jordan, J., Morrison, A., and Senn, W. (2023). NMDA-driven dendritic modulation enables multitask representation learning in hierarchical sensory processing pathways. Proc Natl Acad Sci U S A *120*, e2300558120. 10.1073/pnas.2300558120.
12. Poleg-Polsky, A. (2019). Dendritic Spikes Expand the Range of Well Tolerated Population Noise Structures. J Neurosci *39*, 9173-9184. 10.1523/JNEUROSCI.0638-19.2019.
13. Leugering, J., Nieters, P., and Pipa, G. (2023). Dendritic plateau potentials can process spike sequences across multiple time-scales. Frontiers in Cognition *2*. 10.3389/fcogn.2023.1044216.
14. Gidon, A., Zolnik, T.A., Fidzinski, P., Bolduan, F., Papoutsi, A., Poirazi, P., Holtkamp, M., Vida, I., and Larkum, M.E. (2020). Dendritic action potentials and computation in human layer 2/3 cortical neurons. Science *367*, 83-87.
15. Magó, A., Kis, N., Lükő, B., and Makara, J.K. (2021). Distinct dendritic Ca2+ spike forms produce opposing input-output transformations in rat CA3 pyramidal cells. elife *10*, e74493.
16. Cornford, J.H., Mercier, M.S., Leite, M., Magloire, V., Hausser, M., and Kullmann, D.M. (2019). Dendritic NMDA receptors in parvalbumin neurons enable strong and stable neuronal assemblies. Elife *8*. 10.7554/eLife.49872.
17. Larkum, M.E., Nevian, T., Sandler, M., Polsky, A., and Schiller, J. (2009). Synaptic integration in tuft dendrites oflLayer 5 pyramidal neurons: a new unifying principle. Science *325*, 756-760.
18. Katona, G., Kaszas, A., Turi, G.F., Hajos, N., Tamas, G., Vizi, E.S., and Rozsa, B. (2011). Roller Coaster Scanning reveals spontaneous triggering of dendritic spikes in CA1 interneurons. Proc Natl Acad Sci U S A *108*, 2148-2153. 10.1073/pnas.1009270108.

19. Tran-Van-Minh, A., Abrahamsson, T., Cathala, L., and DiGregorio, D.A. (2016). Differential Dendritic Integration of Synaptic Potentials and Calcium in Cerebellar Interneurons. Neuron *91*, 837-850. 10.1016/j.neuron.2016.07.029.
20. Masala, N., Pofahl, M., Haubrich, A.N., Sameen Islam, K.U., Nikbakht, N., Pasdarnavab, M., Bohmbach, K., Araki, K., Kamali, F., Henneberger, C., et al. (2023). Targeting aberrant dendritic integration to treat cognitive comorbidities of epilepsy. Brain *146*, 2399-2417. 10.1093/brain/awac455.
21. Chiovini, B., Turi, G.F., Katona, G., Kaszas, A., Palfi, D., Maak, P., Szalay, G., Szabo, M.F., Szabo, G., Szadai, Z., et al. (2014). Dendritic spikes induce ripples in parvalbumin interneurons during hippocampal sharp waves. Neuron *82*, 908-924. 10.1016/j.neuron.2014.04.004.
22. Testa-Silva, G., Rosier, M., Honnuraiah, S., Guzulaitis, R., Megias, A.M., French, C., King, J., Drummond, K., Palmer, L.M., and Stuart, G.J. (2022). High synaptic threshold for dendritic NMDA spike generation in human layer 2/3 pyramidal neurons. Cell Rep *41*, 111787. 10.1016/j.celrep.2022.111787.
23. Lafourcade, M., van der Goes, M.H., Vardalaki, D., Brown, N.J., Voigts, J., Yun, D.H., Kim, M.E., Ku, T., and Harnett, M.T. (2022). Differential dendritic integration of long-range inputs in association cortex via subcellular changes in synaptic AMPA-to-NMDA receptor ratio. Neuron *110*, 1532-1546 e1534. 10.1016/j.neuron.2022.01.025.
24. Losonczy, A., and Magee, J.C. (2006). Integrative properties of radial oblique dendrites in hippocampal CA1 pyramidal neurons. Neuron *50*, 291-307. 10.1016/j.neuron.2006.03.016.
25. Camire, O., Lazarevich, I., Gilbert, T., and Topolnik, L. (2018). Mechanisms of Supralinear Calcium Integration in Dendrites of Hippocampal CA1 Fast-Spiking Cells. Front Synaptic Neurosci *10*, 47. 10.3389/fnsyn.2018.00047.
26. Camire, O., and Topolnik, L. (2014). Dendritic calcium nonlinearities switch the direction of synaptic plasticity in fast-spiking interneurons. J Neurosci *34*, 3864-3877. 10.1523/JNEUROSCI.2253-13.2014.
27. Branco, T., and Hausser, M. (2011). Synaptic integration gradients in single cortical pyramidal cell dendrites. Neuron *69*, 885-892. 10.1016/j.neuron.2011.02.006.
28. Ariav, G., Polsky, A., and Schiller, J. (2003). Submillisecond precision of the input–output transformation function mediated by fast sodium dendritic spikes in basal dendrites of CA1 pyramidal neurons. Neuroscience *23*, 7750-7758.
29. Harnett, M.T., Xu, N.L., Magee, J.C., and Williams, S.R. (2013). Potassium channels control the interaction between active dendritic integration compartments in layer 5 cortical pyramidal neurons. Neuron *79*, 516-529. 10.1016/j.neuron.2013.06.005.
30. Hoffman, D.A., Magee, J.C., Colbert, C.M., and Johnston, D. (1997). K+ channel regulation of signal propagation in dendrites of hippocampal pyramidal neurons. Nature *387*, 869-875.
31. Harvey, J., and Collingridge, G.L. (1992). Thapsigargin blocks the induction of long-term potentiation in rat hippocampal slices. Neurosci Lett *139*, 197-200.
32. Padamsey, Z., Foster, W.J., and Emptage, N.J. (2019). Intracellular Ca(2+) Release and Synaptic Plasticity: A Tale of Many Stores. Neuroscientist *25*, 208-226. 10.1177/1073858418785334.
33. Freund, T.F., and Buzsáki, G. (1998). Interneurons of the hippocampus. Hippocampus *6*, 347-470. 10.1002/(sici)1098-1063(1996)6:4<347::Aid-hipo1>3.0.Co;2-i.
34. Hertag, L., and Sprekeler, H. (2020). Learning prediction error neurons in a canonical interneuron circuit. Elife *9*. 10.7554/eLife.57541.
35. Tzilivaki, A., Tukker, J.J., Maier, N., Poirazi, P., Sammons, R.P., and Schmitz, D. (2023). Hippocampal GABAergic interneurons and memory. Neuron *111*, 3154-3175. 10.1016/j.neuron.2023.06.016.
36. Hu, H., and Vervaeke, K. (2018). Synaptic integration in cortical inhibitory neuron dendrites. Neuroscience *368*, 115-131. 10.1016/j.neuroscience.2017.06.065.
37. Kriener, B., Hu, H., and Vervaeke, K. (2022). Parvalbumin interneuron dendrites enhance gamma oscillations. Cell Rep *39*, 110948. 10.1016/j.celrep.2022.110948.

38. Dinocourt, C., Petanjek, Z., Freund, T.F., Ben-Ari, Y., and Esclapez, M. (2003). Loss of interneurons innervating pyramidal cell dendrites and axon initial segments in the CA1 region of the hippocampus following pilocarpine-induced seizures. J Comp Neurol *459*, 407-425. 10.1002/cne.10622.
39. Fujiwara-Tsukamoto, Y., Isomura, Y., Imanishi, M., Ninomiya, T., Tsukada, M., Yanagawa, Y., Fukai, T., and Takada, M. (2010). Prototypic seizure activity driven by mature hippocampal fast-spiking interneurons. J Neurosci *30*, 13679-13689. 10.1523/JNEUROSCI.1523-10.2010.
40. Magloire, V., Mercier, M.S., Kullmann, D.M., and Pavlov, I. (2019). GABAergic Interneurons in Seizures: Investigating Causality With Optogenetics. Neuroscientist *25*, 344-358. 10.1177/1073858418805002.
41. Marx, M., Haas, C.A., and Haussler, U. (2013). Differential vulnerability of interneurons in the epileptic hippocampus. Front Cell Neurosci *7*, 167. 10.3389/fncel.2013.00167.
42. Belforte, J.E., Zsiros, V., Sklar, E.R., Jiang, Z., Yu, G., Li, Y., Quinlan, E.M., and Nakazawa, K. (2010). Postnatal NMDA receptor ablation in corticolimbic interneurons confers schizophrenia-like phenotypes. Nat Neurosci *13*, 76-83. 10.1038/nn.2447.
43. Jahangir, M., Zhou, J.S., Lang, B., and Wang, X.P. (2021). GABAergic System Dysfunction and Challenges in Schizophrenia Research. Front Cell Dev Biol *9*, 663854. 10.3389/fcell.2021.663854.
44. Marin, O. (2012). Interneuron dysfunction in psychiatric disorders. Nat Rev Neurosci *13*, 107-120. 10.1038/nrn3155.
45. Lunden, J.W., Durens, M., Phillips, A.W., and Nestor, M.W. (2019). Cortical interneuron function in autism spectrum condition. Pediatr Res *85*, 146-154. 10.1038/s41390-018-0214-6.
46. Hijazi, S., Heistek, T.S., Scheltens, P., Neumann, U., Shimshek, D.R., Mansvelder, H.D., Smit, A.B., and van Kesteren, R.E. (2020). Early restoration of parvalbumin interneuron activity prevents memory loss and network hyperexcitability in a mouse model of Alzheimer's disease. Mol Psychiatry *25*, 3380-3398. 10.1038/s41380-019-0483-4.
47. Verret, L., Mann, E.O., Hang, G.B., Barth, A.M., Cobos, I., Ho, K., Devidze, N., Masliah, E., Kreitzer, A.C., Mody, I., et al. (2012). Inhibitory interneuron deficit links altered network activity and cognitive dysfunction in Alzheimer model. Cell *149*, 708-721. 10.1016/j.cell.2012.02.046.
48. Pelkey, K.A., Chittajallu, R., Craig, M.T., Tricoire, L., Wester, J.C., and McBain, C.J. (2017). Hippocampal GABAergic Inhibitory Interneurons. Physiol Rev *97*, 1619-1747. 10.1152/physrev.00007.2017.
49. Mitchell, D.E., Miranda-Rottmann, S., Blanchard, M., and Araya, R. (2023). Altered integration of excitatory inputs onto the basal dendrites of layer 5 pyramidal neurons in a mouse model of Fragile X syndrome. Proc Natl Acad Sci U S A *120*, e2208963120. 10.1073/pnas.2208963120.
50. Griesius, S., O'Donnell, C., Waldron, S., Thomas, K.L., Dwyer, D.M., Wilkinson, L.S., Hall, J., Robinson, E.S.J., and Mellor, J.R. (2022). Reduced expression of the psychiatric risk gene DLG2 (PSD93) impairs hippocampal synaptic integration and plasticity. Neuropsychopharmacology *47*, 1367-1378. 10.1038/s41386-022-01277-6.
51. Nelson, A.D., and Bender, K.J. (2021). Dendritic Integration Dysfunction in Neurodevelopmental Disorders. Dev Neurosci *43*, 201-221. 10.1159/000516657.
52. Palmer, L.M. (2014). Dendritic integration in pyramidal neurons during network activity and disease. Brain Res Bull *103*, 2-10. 10.1016/j.brainresbull.2013.09.010.
53. Asgarian, Z., Magno, L., Ktena, N., Harris, K.D., and Kessaris, N. (2019). Hippocampal CA1 Somatostatin Interneurons Originate in the Embryonic MGE/POA. Stem Cell Reports *13*, 793-802. 10.1016/j.stemcr.2019.09.008.
54. Booker, S.A., and Wyllie, D.J.A. (2021). NMDA receptor function in inhibitory neurons. Neuropharmacology *196*, 108609. 10.1016/j.neuropharm.2021.108609.
55. Sik, A., Penttonen, M., Ylinen, A., and Buzsáki, G. (1995). Hippocampal CA1 interneurons: an in vivo intracellular labeling study J Neurosci *15*, 6651-6665.

56. Chittajallu, R., Wester, J.C., Craig, M.T., Barksdale, E., Yuan, X.Q., Akgul, G., Fang, C., Collins, D., Hunt, S., Pelkey, K.A., and McBain, C.J. (2017). Afferent specific role of NMDA receptors for the circuit integration of hippocampal neurogliaform cells. Nat Commun *8*, 152. 10.1038/s41467-017-00218-y.
57. Price, C.J., Cauli, B., Kovacs, E.R., Kulik, A., Lambolez, B., Shigemoto, R., and Capogna, M. (2005). Neurogliaform neurons form a novel inhibitory network in the hippocampal CA1 area. J Neurosci *25*, 6775-6786. 10.1523/JNEUROSCI.1135-05.2005.
58. Tricoire, L., Pelkey, K.A., Daw, M.I., Sousa, V.H., Miyoshi, G., Jeffries, B., Cauli, B., Fishell, G., and McBain, C.J. (2010). Common origins of hippocampal Ivy and nitric oxide synthase expressing neurogliaform cells. J Neurosci *30*, 2165-2176. 10.1523/JNEUROSCI.5123-09.2010.
59. Mercier, M.S., Magloire, V., Cornford, J.H., and Kullmann, D.M. (2022). Long-term potentiation in neurogliaform interneurons modulates excitation-inhibition balance in the temporoammonic pathway. J Physiol *600*, 4001-4017. 10.1113/JP282753.
60. Booker, S.A., and Vida, I. (2018). Morphological diversity and connectivity of hippocampal interneurons. Cell Tissue Res *373*, 619-641. 10.1007/s00441-018-2882-2.
61. Taniguchi, H., He, M., Wu, P., Kim, S., Paik, R., Sugino, K., Kvitsiani, D., Fu, Y., Lu, J., Lin, Y., et al. (2011). A resource of Cre driver lines for genetic targeting of GABAergic neurons in cerebral cortex. Neuron *71*, 995-1013. 10.1016/j.neuron.2011.07.026.
62. Chen, T.W., Wardill, T.J., Sun, Y., Pulver, S.R., Renninger, S.L., Baohan, A., Schreiter, E.R., Kerr, R.A., Orger, M.B., Jayaraman, V., et al. (2013). Ultrasensitive fluorescent proteins for imaging neuronal activity. Nature *499*, 295-300. 10.1038/nature12354.
63. Buzsáki, G., and Kandel, A. (1998). Somadendritic backpropagation of action potentials in cortical pyramidal cells of the awake rat. Neurophysiol *79*, 1587-1591.
64. Stuart, G., and Sakmann, B. (1994). Active propagation of somatic action potentials into neocortical pyramidal cell dendrites. Nature *367*, 69–72.
65. Stuart, G., Schiller, J., and Sakmann, B. (1997). Action potential initiation and propagation in rat neocortical pyramidal neurons. J Physiol *505 (Pt 3)*, 617-632. 10.1111/j.1469-7793.1997.617ba.x.
66. Armstrong, C., Szabadics, J., Tamas, G., and Soltesz, I. (2011). Neurogliaform cells in the molecular layer of the dentate gyrus as feed-forward gamma-aminobutyric acidergic modulators of entorhinal-hippocampal interplay. J Comp Neurol *519*, 1476-1491. 10.1002/cne.22577.
67. Martina, M., Vida, I., and Jonas, P. (2000). Distal initiation and active propagation of action potentials in interneuron dendrites. Science *287*, 295-300.
68. Maccaferri, G., Roberts, J.D., Szucs, P., Cottingham, C.A., and Somogyi, P. (2000). Cell surface domain specific postsynaptic currents evoked by identified GABAergic neurones in rat hippocampus in vitro. J Physiol *524*, 91-116. 10.1111/j.1469-7793.2000.t01-3-00091.x.
69. Iacaruso, M.F., Gasler, I.T., and Hofer, S.B. (2017). Synaptic organization of visual space in primary visual cortex. Nature *547*, 449-452. 10.1038/nature23019.
70. Takahashi, N., Kitamura, K., Matsuo, N., Mayford, M., Kano, M., Matsuki, N., and Ikegaya, Y. (2012). Locally synchronized synaptic inputs. Science *335*, 353-356. 10.1126/science.1210362.
71. Wilson, D.E., Whitney, D.E., Scholl, B., and Fitzpatrick, D. (2016). Orientation selectivity and the functional clustering of synaptic inputs in primary visual cortex. Nat Neurosci *19*, 1003-1009. 10.1038/nn.4323.
72. Kullmann, D.M., Moreau, A.W., Bakiri, Y., and Nicholson, E. (2012). Plasticity of inhibition. Neuron *75*, 951-962. 10.1016/j.neuron.2012.07.030.
73. Tasic, B., Menon, V., Nguyen, T.N., Kim, T.K., Jarsky, T., Yao, Z., Levi, B., Gray, L.T., Sorensen, S.A., Dolbeare, T., et al. (2016). Adult mouse cortical cell taxonomy revealed by single cell transcriptomics. Nat Neurosci *19*, 335-346. 10.1038/nn.4216.
74. Madisen, L., Zwingman, T.A., Sunkin, S.M., Oh, S.W., Zariwala, H.A., Gu, H., Ng, L.L., Palmiter, R.D., Hawrylycz, M.J., Jones, A.R., et al. (2010). A robust and high-throughput Cre reporting

and characterization system for the whole mouse brain. Nat Neurosci *13*, 133-140. 10.1038/nn.2467.

75. Schmidt-Hieber, C., Toleikyte, G., Aitchison, L., Roth, A., Clark, B.A., Branco, T., and Hausser, M. (2017). Active dendritic integration as a mechanism for robust and precise grid cell firing. Nat Neurosci *20*, 1114-1121. 10.1038/nn.4582.
76. Claridge-Chang, A., and Assam, P.N. (2016). Estimation statistics should replace significance testing. Nat Methods *13*, 108-109. 10.1038/nmeth.3729.
77. Ho, J., Tumkaya, T., Aryal, S., Choi, H., and Claridge-Chang, A. (2019). Moving beyond P values: data analysis with estimation graphics. Nat Methods *16*, 565-566. 10.1038/s41592-019-0470-3.
78. Gohlke, C. (2022). Oiffile Read Olympus(r) image files (OIF and OIB). https://github.com/cgohlke/oiffile/.
79. Garcia, S., Guarino, D., Jaillet, F., Jennings, T., Propper, R., Rautenberg, P.L., Rodgers, C.C., Sobolev, A., Wachtler, T., Yger, P., and Davison, A.P. (2014). Neo: an object model for handling electrophysiology data in multiple formats. Front Neuroinform *8*, 10. 10.3389/fninf.2014.00010.

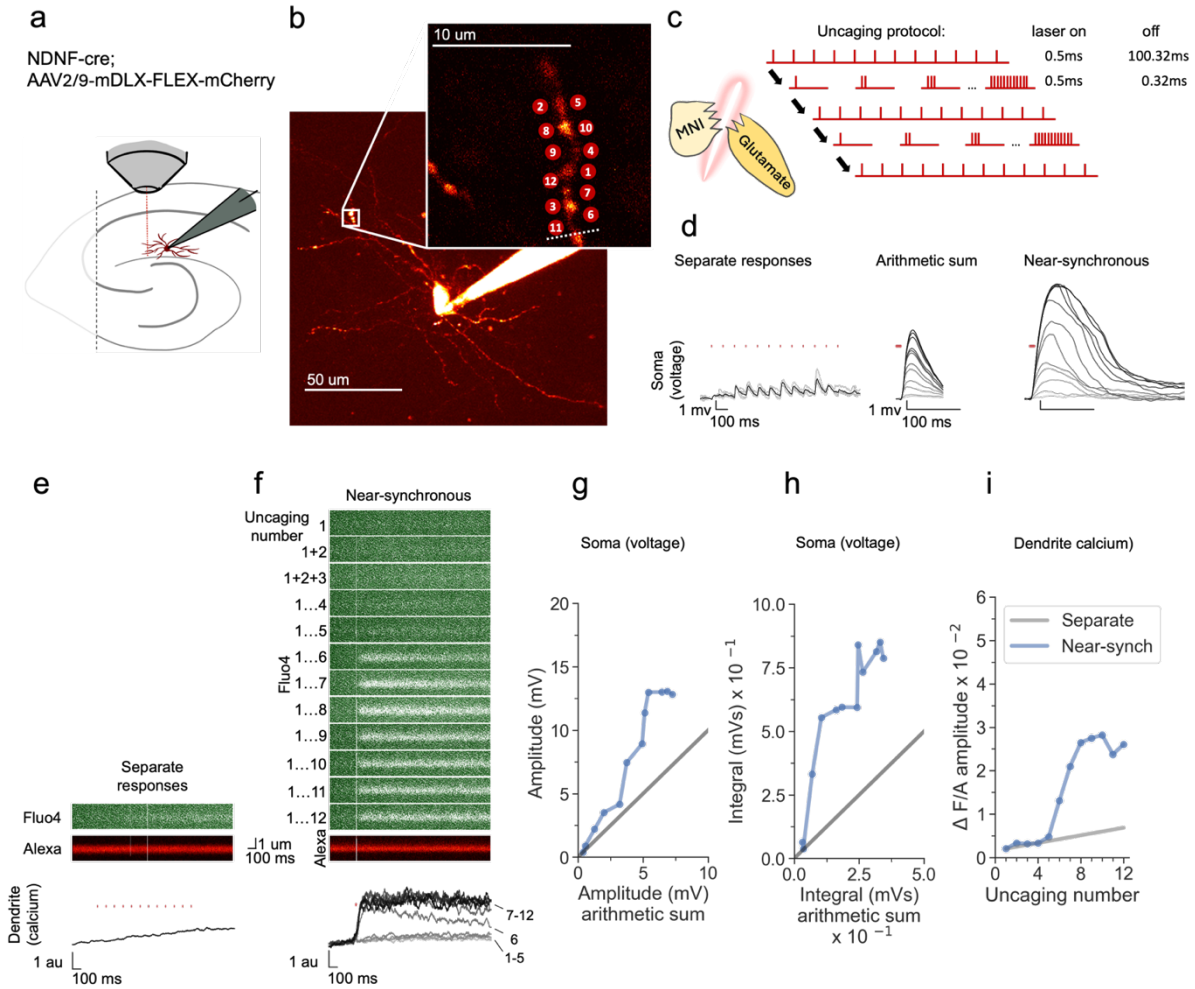
a
NDNF-cre;
AAV2/9-mDLX-FLEX-mCherry
b
10 um
50 um
c
Uncaging protocol:
laser on
off
0.5ms
100.32ms
0.5ms
0.32ms
MNI
Glutamate
d
Separate responses
Arithmetic sum
Near-synchronous
Soma (voltage)
1 mv
100 ms
e
Separate responses
Fluo4
Alexa
Dendrite (calcium)
1 au
100 ms
f
Near-synchronous
Uncaging number
1
1+2
1+2+3
1...4
1...5
1...6
1...7
1...8
1...9
1...10
1...11
1...12
Fluo4
Alexa
1 um
100 ms
7-12
6
1-5
1 au
100 ms
g
Soma (voltage)
Amplitude (mV)
Amplitude (mV) arithmetic sum
h
Soma (voltage)
Integral (mVs) x 10 −1
Integral (mVs) arithmetic sum x 10 −1
i
Dendrite calcium)
Separate
Near-synch
Δ F/A amplitude x 10 −2
Uncaging number

Fig 1. Experimental overview and representative example showing supralinear dendritic integration in a neurogliaform interneuron.

(a) Summary depicting the mouse model, viral expression, and acute slice preparation with patch-clamp and imaging and uncaging.

(b) Alexa-594 fluorescence Z-stack of a representative neurogliaform NDNF+ interneuron, with uncaging locations and the position of the linescan used to measure dendritic calcium transients (dotted white line)(inset). The image was obtained after the experiment was concluded.

(c) Uncaging protocol for asynchronous (separate responses) and near-synchronous conditions.

(d) Representative somatic voltage traces across asynchronous separate response and near-synchronous conditions. Laser uncaging light stimuli are indicated by red dots above the traces. uEPSPs were elicited in the asynchronous condition with light pulses separated by an interval of 100.32 ms (left; grey traces: individual sweeps; black traces average). The arithmetic sum traces were calculated by aligning and summing an increasing number of asynchronously evoked responses (middle). Near-synchronous uEPSPs were elicited with light pulses separated by an interval of 0.32 ms (right). The families of traces for the arithmetic sum and near-synchronously evoked responses are shown as light to dark grey traces, indicating an increase in the number of uncaging loci from 1 to 12.

(e) Fluo-4 and Alexa-594 linescans during asynchronous sequential uncaging at 12 loci at times indicated by the vertical red dashes. The ratio of dendritic Fluo-4 to Alexa fluorescence is shown below (au: arbitrary unit).

(f) Linescans during near-synchronous uncaging at increasing numbers of locations (1 – 12, top to bottom).

(g) Peak amplitude of the recorded near-synchronous response plotted against the amplitude of the arithmetic sum as the number of uncaging loci was increased.

(h) Time integral of the recorded near-synchronous response plotted against the integral of the arithmetic sum.

(i) Fluo-4 fluorescence transient amplitude, normalised by Alexa-594 fluorescence, plotted against the number of locations uncaged near-synchronously. The grey line indicates the estimated separate response amplitude interpolated from the fluorescence measured between 1 and 12 locations uncaged asynchronously (see Methods).

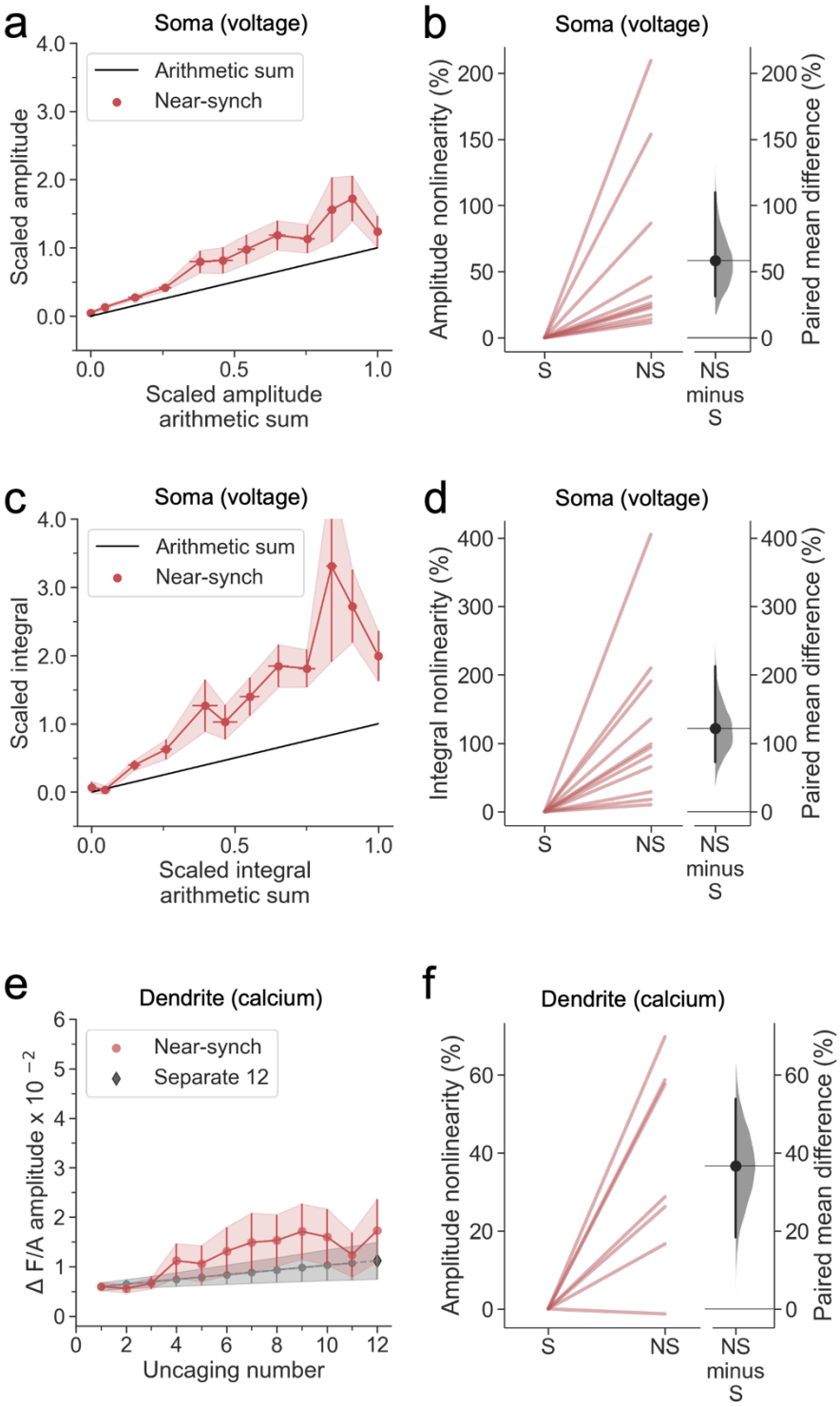
a
Soma (voltage)
Arithmetic sum
Near-synch
Scaled amplitude
Scaled amplitude arithmetic sum
b
Soma (voltage)
Amplitude nonlinearity (%)
Paired mean difference (%)
S
NS
NS minus S
c
Soma (voltage)
Arithmetic sum
Near-synch
Scaled integral
Scaled integral arithmetic sum
d
Soma (voltage)
Integral nonlinearity (%)
Paired mean difference (%)
S
NS
NS minus S
e
Dendrite (calcium)
Near-synch
Separate 12
Δ F/A amplitude x 10 −2
Uncaging number
f
Dendrite (calcium)
Amplitude nonlinearity (%)
Paired mean difference (%)
S
NS
NS minus S

Fig. 2. Summary of supralinear dendritic integration in neurogliaform interneurons.

(a) Average scaled amplitude of recorded near-synchronous uEPSPs plotted against scaled amplitude of the arithmetic sum of asynchronously evoked uEPSPs as the cumulative number of uncaging locations was increased (n=11 dendrites in 11 cells from 9 animals; error bars represent SEM)..

(b) Amplitude nonlinearity quantified for data shown in (a). The paired mean difference between near-synchronous (NS) and asynchronous separate responses (S) is 56% [95%CI 27%, 108%]. P<0.001 (two-sided permutation t-test compared to 0%).

(c) Average scaled near-synchronous uEPSP integral plotted against scaled arithmetic sum of asynchronous separate responses, for the same dataset.

(d) Integral nonlinearity corresponding to panel (c). The paired mean difference between near-synchronous (NS) and asynchronous separate responses (S) is 122% [95%CI 73%, 213%]. P<0.001 (two-sided permutation t-test compared to 0%).

(e) Average Fluo-4/Alexa-594 fluorescence transients plotted against the cumulative number of uncaging locations. The grey line indicates the interpolated values used in the nonlinearity calculation (see Methods). The dark grey diamond indicates the amplitude from the 12th asynchronous response. (n = 7 dendrites in 7 cells from 7 animals).

(f) Amplitude nonlinearity corresponding to panel (c) (dendritic calcium). The paired mean difference between near-synchronous (NS) and asynchronous separate responses (S) is 37% [95%CI 18%, 54%]. P=0.0138 (two-sided permutation t-test compared to 0%).

For the slopegraphs and Gardner-Altman estimation plots, paired observations are connected by coloured lines. The paired mean differences between the near-synchronous (NS) and asynchronous separate response (S) groups are shown in Gardner-Altman estimation plots as bootstrap sampling distributions. The mean differences are depicted as black dots. The 95% confidence intervals are indicated by the ends of the vertical error bars.

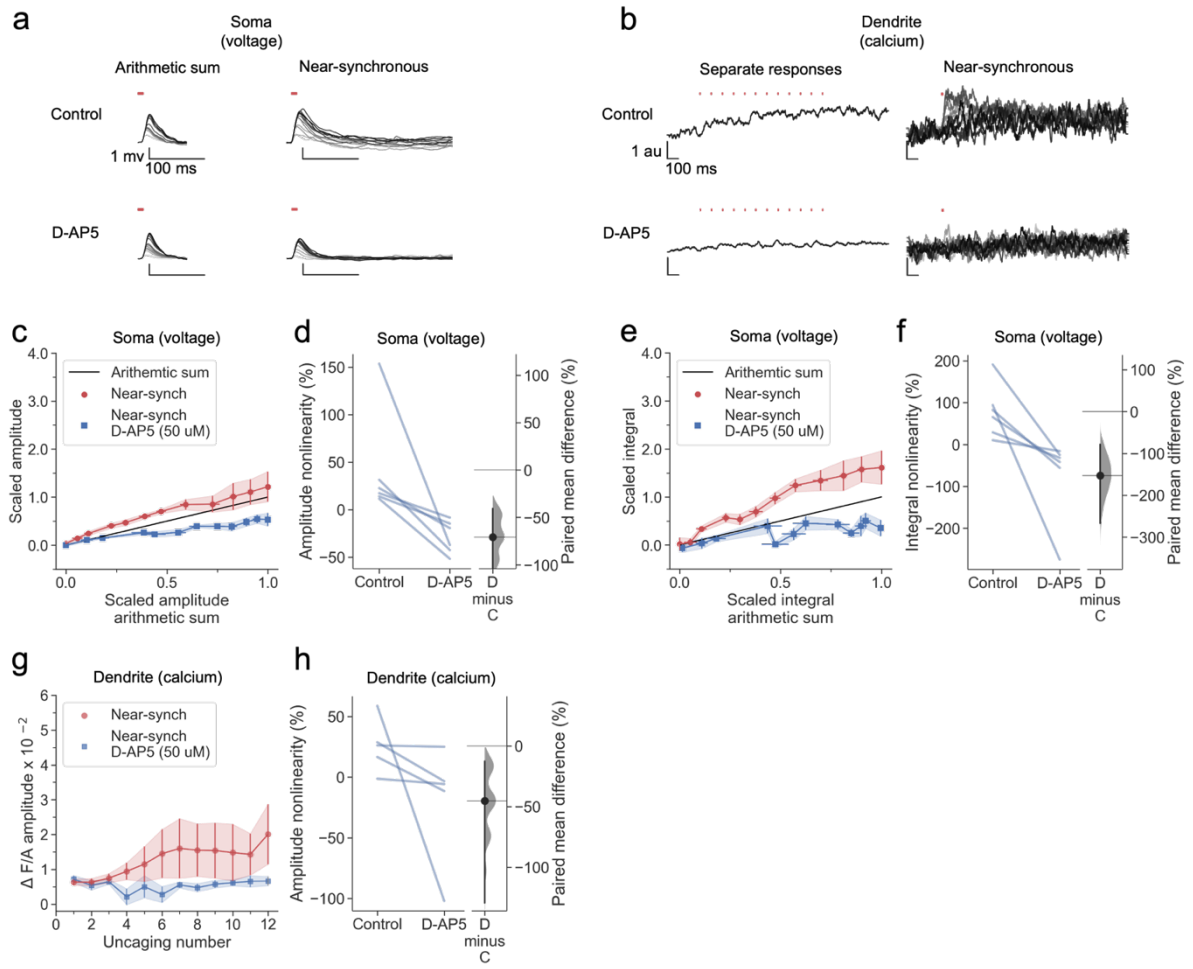
a
Soma (voltage)
Arithmetic sum
Near-synchronous
Control
1 mv
100 ms
D-AP5
b
Dendrite (calcium)
Separate responses
Near-synchronous
Control
1 au
100 ms
D-AP5
c
Soma (voltage)
Arithemtic sum
Near-synch
Near-synch D-AP5 (50 uM)
Scaled amplitude
Scaled amplitude arithmetic sum
d
Soma (voltage)
Amplitude nonlinearity (%)
Paired mean difference (%)
Control
D-AP5
D minus C
e
Soma (voltage)
Arithemtic sum
Near-synch
Near-synch D-AP5 (50 uM)
Scaled integral
Scaled integral arithmetic sum
f
Soma (voltage)
Integral nonlinearity (%)
Paired mean difference (%)
Control
D-AP5
D minus C
g
Dendrite (calcium)
Near-synch
Near-synch D-AP5 (50 uM)
Δ F/A amplitude x 10 −2
Uncaging number
h
Dendrite (calcium)
Amplitude nonlinearity (%)
Paired mean difference (%)
Control
D-AP5
D minus C

Fig. 3. Sublinear dendritic integration in neurogliaform interneurons with NMDARs blocked.

(a) Somatic uEPSPs evoked by uncaging glutamate in a representative neuron before (top) and after (bottom) D-AP5 (50 uM) perfusion. Uncaging protocol and data representation as in Figs. 1-2.

(b) Dendritic Fluo-4 traces in the same neuron, in response to asynchronous and near-synchronous uncaging, before (left) and after NMDAR blockade (right).

(c) Scaled amplitude of the recorded near-synchronous uEPSP plotted against scaled amplitude of the arithmetic sum, as the number of uncaging locations was increased. Error bars: SEM (n=6 dendrites in 6 cells from 6 animals). The supralinear relationship became sublinear with NMDARs blocked.

(d) Amplitude nonlinearity for individual neurons shown in (c) before and after D-AP5 perfusion. The paired mean difference between the two conditions is -71% [95%CI -147%, -41%]. P<0.001 (two-sided permutation t-test).

(e) Scaled time-integral of uEPSPs plotted against scaled integral arithmetic sum of asynchronous separate responses, before and after NMDAR blockade.

(f) Integral nonlinearity corresponding to panel (e). The paired mean difference between baseline and D-AP5 conditions is -153% [95%CI -267%, -78%]. P <0.001 (two-sided permutation t-test).

(g) Fluo-4 fluorescence transients (normalised to Alexa-594) plotted against the cumulative number of uncaging locations, before and after NMDAR blockade. Data plotted as in Fig. 1.

(h) Amplitude nonlinearity corresponding to panel (g). The paired mean difference between baseline and D-AP5 conditions is -45% [95%CI -129%, -13%]. P<0.001 (two-sided permutation t-test).

Slopegraphs and Gardner-Altman estimation plots as in Fig. 2.

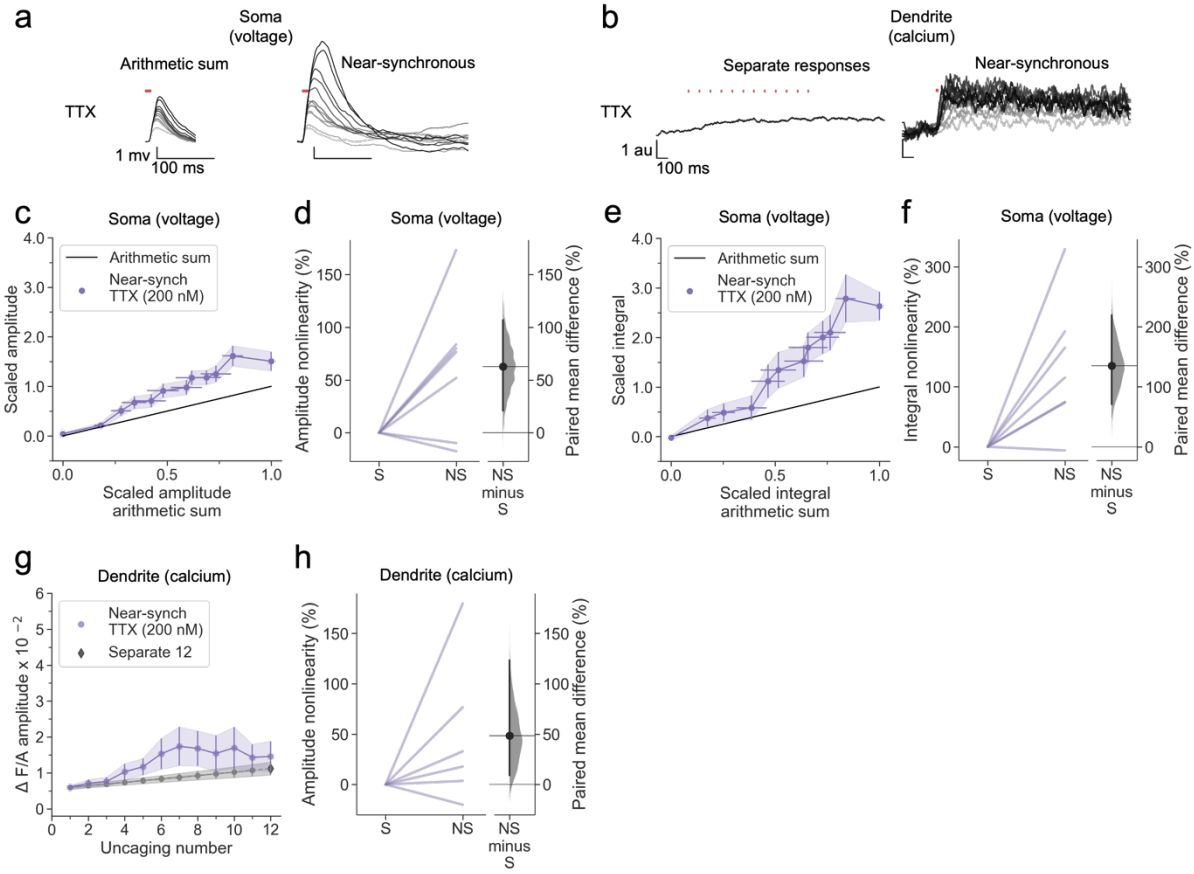
a
Soma (voltage)
Arithmetic sum
Near-synchronous
TTX
1 mv
100 ms
b
Dendrite (calcium)
Separate responses
Near-synchronous
TTX
1 au
100 ms
c
Soma (voltage)
Arithmetic sum
Near-synch TTX (200 nM)
Scaled amplitude
Scaled amplitude arithmetic sum
d
Soma (voltage)
Amplitude nonlinearity (%)
Paired mean difference (%)
S
NS
NS minus S
e
Soma (voltage)
Arithmetic sum
Near-synch TTX (200 nM)
Scaled integral
Scaled integral arithmetic sum
f
Soma (voltage)
Integral nonlinearity (%)
Paired mean difference (%)
S
NS
NS minus S
g
Dendrite (calcium)
Near-synch TTX (200 nM)
Separate 12
Δ F/A amplitude x 10 −2
Uncaging number
h
Dendrite (calcium)
Amplitude nonlinearity (%)
Paired mean difference (%)
S
NS
NS minus S

Fig. 4. Supralinear dendritic integration in neurogliaform interneurons does not require voltage-dependent sodium channels.

(a) Somatic uEPSPs evoked by uncaging glutamate in a representative neuron in the presence of TTX (200 nM), showing supralinear summation.

(b) Dendritic Fluo-4 fluorescence responses in the same neuron, showing supralinear calcium signalling.

(c) Average scaled amplitude of recorded near-synchronous uEPSP plotted against scaled amplitude arithmetic sum with increasing numbers of cumulative uncaging locations (n=7 dendrites in 5 cells from 5 animals).

(d) Amplitude nonlinearity corresponding to panel (c). The paired mean difference between near-synchronous (NS) and asynchronous separate responses (S) is 63% [95%CI 21%, 107%]. P=0.0382 (two-sided permutation t-test compared to 0%).

(e) uEPSP amplitude nonlinearity quantified by integral, plotted in the same way as (c).

(f) Integral nonlinearity corresponding to (e). The paired mean difference between near-synchronous (NS) and asynchronous separate responses (S) is 135% [95%CI 71%, 220%]. P=0.011 (two-sided permutation t-test compared to 0%).

(g) Fluo-4 fluorescence transient amplitude (normalised to Alexa-594) plotted against the cumulative number of uncaging locations. Data plotted as in Fig. 1.

(h) Amplitude nonlinearity corresponding to panel (g). The paired mean difference between near-synchronous (NS) and asynchronous separate responses (S) is 48% [95%CI 9%, 123%]. P=0.088 (two-sided permutation t-test compared to 0%).

Slopegraphs and Gardner-Altman estimation plots as in Fig. 2.

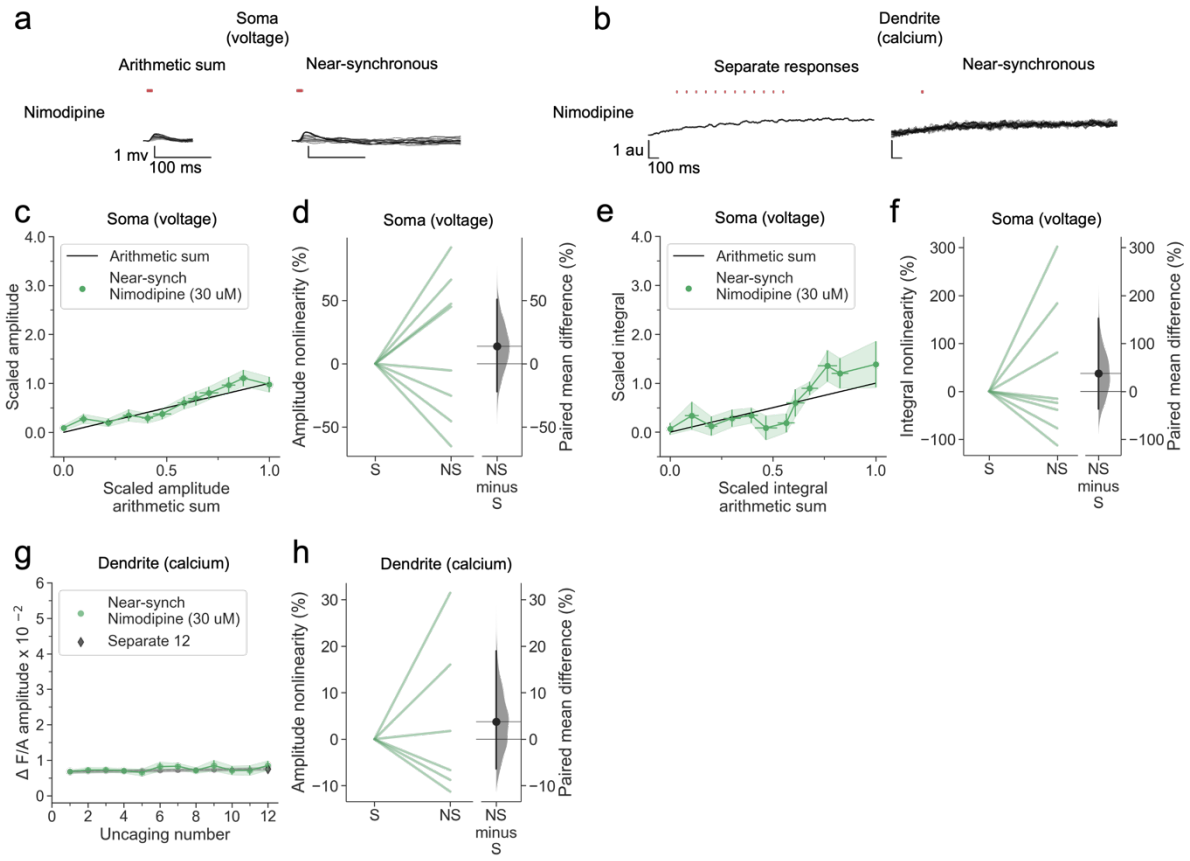
a
Soma (voltage)
Arithmetic sum
Near-synchronous
Nimodipine
1 mv
100 ms
b
Dendrite (calcium)
Separate responses
Near-synchronous
Nimodipine
1 au
100 ms
c
Soma (voltage)
Arithmetic sum
Near-synch
Nimodipine (30 uM)
Scaled amplitude
Scaled amplitude arithmetic sum
d
Soma (voltage)
Amplitude nonlinearity (%)
Paired mean difference (%)
S
NS
NS minus S
e
Soma (voltage)
Arithmetic sum
Near-synch
Nimodipine (30 uM)
Scaled integral
Scaled integral arithmetic sum
f
Soma (voltage)
Integral nonlinearity (%)
Paired mean difference (%)
S
NS
NS minus S
g
Dendrite (calcium)
Near-synch
Nimodipine (30 uM)
Separate 12
Δ F/A amplitude x 10 −2
Uncaging number
h
Dendrite (calcium)
Amplitude nonlinearity (%)
Paired mean difference (%)
S
NS
NS minus S

Fig. 5. L-type voltage-dependent calcium channel blockade abolishes nonlinear dendritic calcium summation.

(a) Somatic uEPSPs evoked by glutamate uncaging in one neuron in the presence of nimodipine (30 uM), showing supralinear uEPSP integration.

(b) Dendritic Fluo-4 fluorescence transients in the same neuron, showing absence of supralinear integration.

(c) Average scaled amplitude of the recorded near-synchronous uEPSP plotted against the arithmetic sum of the scaled asynchronous uEPSPs, as the cumulative number of uncaging locations was increased. Error bars show SEM (n=8 dendrites in 5 cells from 3 animals).

(d) Amplitude nonlinearity corresponding to (c). The paired mean difference between near-synchronous (NS) and asynchronous separate responses (S) is 14% [95%CI -22%, 51%]. P= 0.505 (two-sided permutation t-test compared to 0%).

(e) uEPSP amplitude nonlinearity quantified by integral, plotted in the same way as (c).

(f) Integral nonlinearity corresponding to (e). The paired mean difference between near-synchronous (NS) and asynchronous separate responses (S) is 37% [95%CI -37%, 153%]. P=0.497 (two-sided permutation t-test compared to 0%).

(g) Fluo-4 fluorescence transient amplitude (normalised to Alexa-594) plotted against cumulative number of uncaging locations. Data plotted as in Fig. 1.

(h) Amplitude nonlinearity corresponding to (g). The paired mean difference between near-synchronous (NS) and asynchronous separate responses (S) is 4% [95%CI -6%, 19%]. P=0.561 (two-sided permutation t-test compared to 0%).

Slopegraphs and Gardner-Altman estimation plots as in Fig. 2.

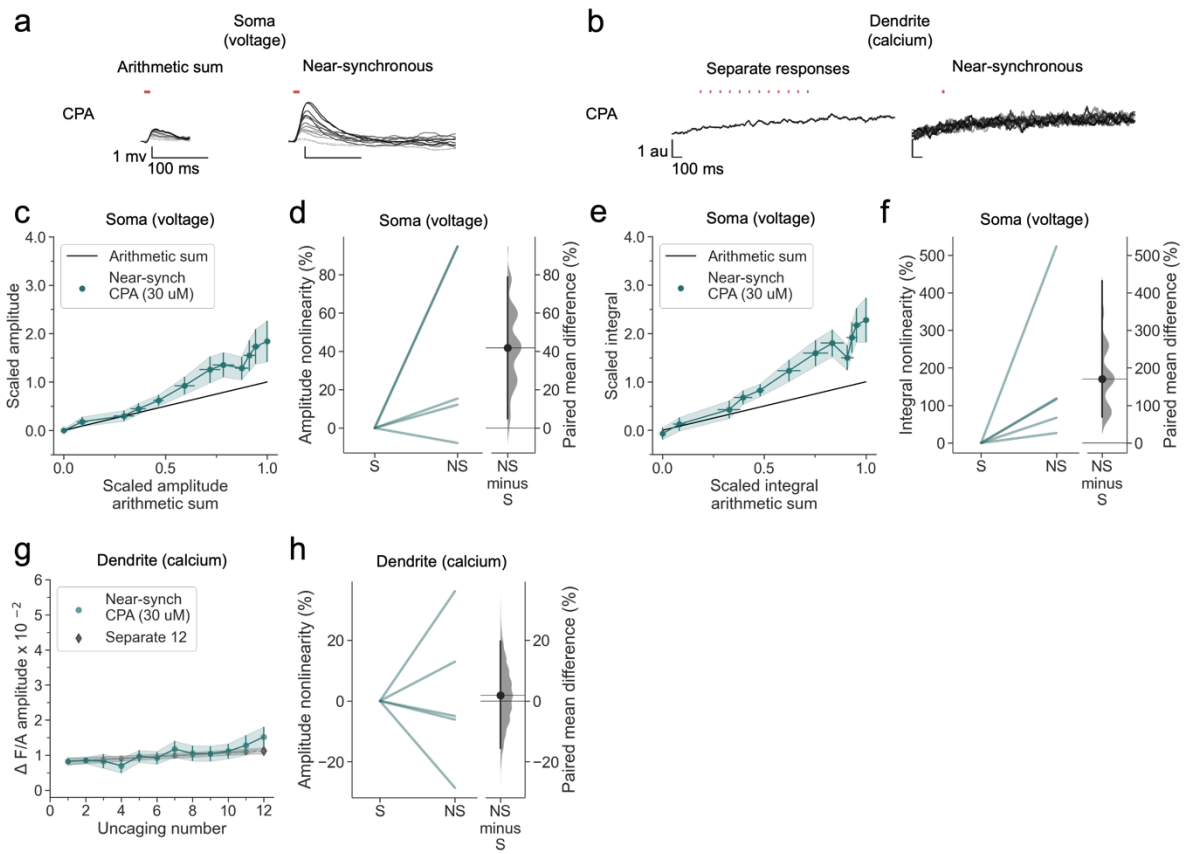
a
Soma (voltage)
Arithmetic sum
Near-synchronous
CPA
1 mv
100 ms
b
Dendrite (calcium)
Separate responses
Near-synchronous
CPA
1 au
100 ms
c
Soma (voltage)
Arithmetic sum
Near-synch CPA (30 uM)
Scaled amplitude
Scaled amplitude arithmetic sum
d
Soma (voltage)
Amplitude nonlinearity (%)
Paired mean difference (%)
S
NS
NS minus S
e
Soma (voltage)
Arithmetic sum
Near-synch CPA (30 uM)
Scaled integral
Scaled integral arithmetic sum
f
Soma (voltage)
Integral nonlinearity (%)
Paired mean difference (%)
S
NS
NS minus S
g
Dendrite (calcium)
Near-synch CPA (30 uM)
Separate 12
Δ F/A amplitude x 10 −2
Uncaging number
h
Dendrite (calcium)
Amplitude nonlinearity (%)
Paired mean difference (%)
S
NS
NS minus S

Fig. 6. SERCA inhibition abolishes nonlinear dendritic calcium summation.

(a) Somatic uEPSPs evoked by glutamate uncaging in one neuron in the presence of CPA (30 uM), showing supralinear uEPSP integration.

(b) Dendritic Fluo-4 fluorescence transients in the same neuron, showing absence of supralinear integration.

(c) Average scaled amplitude of the recorded near-synchronous uEPSP plotted against the arithmetic sum of the scaled asynchronous uEPSPs, as the cumulative number of uncaging locations was increased. Error bars show SEM (n=5 dendrites in 2 cells from 2 animals).

(d) Amplitude nonlinearity corresponding to (c). The paired mean difference between near-synchronous (NS) and asynchronous separate responses (S) is 42% [95%CI 5%, 79%]. P= 0.067 (two-sided permutation t-test compared to 0%).

(e) uEPSP amplitude nonlinearity quantified by integral, plotted in the same way as (c).

(f) Integral nonlinearity corresponding to (e). The paired mean difference between near-synchronous (NS) and asynchronous separate responses (S) is 171% [95%CI 69%, 432%]. P<0.001 (two-sided permutation t-test compared to 0%).

(g) Fluo-4 fluorescence transient amplitude (normalised to Alexa-594) plotted against cumulative number of uncaging locations. Data plotted as in Fig. 1.

(h) Amplitude nonlinearity corresponding to (g). The paired mean difference between near-synchronous (NS) and asynchronous separate responses (S) is 2% [95%CI -16%, 20%]. P=0.754 (two-sided permutation t-test compared to 0%).

Slopegraphs and Gardner-Altman estimation plots as in Fig. 2.

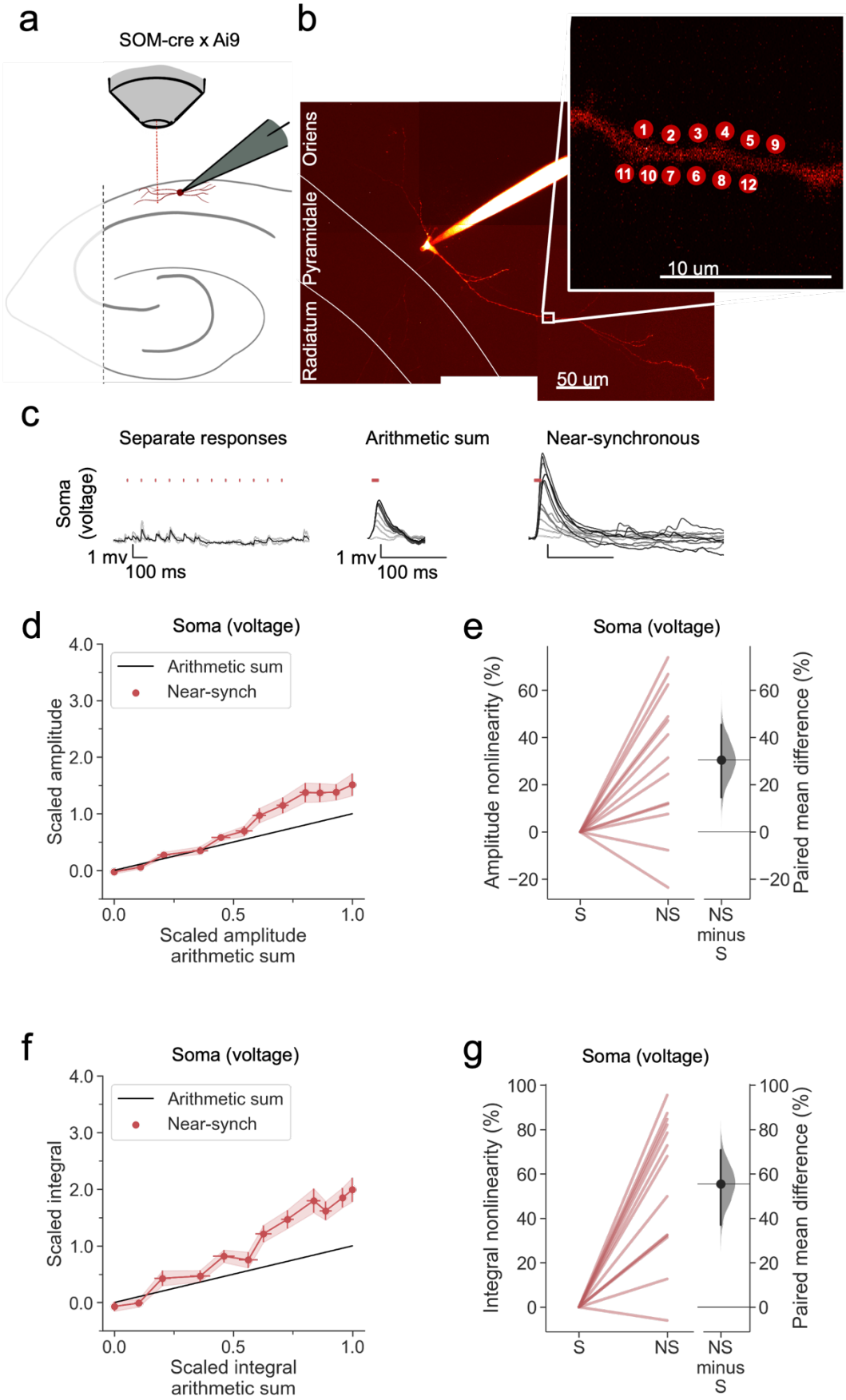
a
SOM-cre x Ai9
b
Oriens
Pyramidale
Radiatum
1
2
3
4
5
9
11
10
7
6
8
12
10 um
50 um
c
Separate responses
Arithmetic sum
Near-synchronous
Soma (voltage)
1 mv
100 ms
1 mv
100 ms
d
Soma (voltage)
Arithmetic sum
Near-synch
Scaled amplitude
Scaled amplitude arithmetic sum
e
Soma (voltage)
Amplitude nonlinearity (%)
Paired mean difference (%)
S
NS
NS minus S
f
Soma (voltage)
Arithmetic sum
Near-synch
Scaled integral
Scaled integral arithmetic sum
g
Soma (voltage)
Integral nonlinearity (%)
Paired mean difference (%)
S
NS
NS minus S

Fig. 7. Supralinear dendritic integration in OLM interneurons.

(a) Summary depicting the mouse model and acute slice preparation with patch-clamp and imaging and uncaging. Uncaging protocol and data representation as in Figs. 1-2

(b) Alexa-594 fluorescence Z-stack of a representative OLM SOM+ interneuron with uncaging locations (inset). The image was obtained after the experiment was concluded.

(c) Representative somatic voltage traces across asynchronous separate response and near-synchronous conditions, depicted as in Fig. 1.

(d) Average scaled amplitude of the recorded near-synchronous uEPSP plotted against the arithmetic sum of the scaled asynchronous uEPSPs, as the cumulative number of uncaging locations was increased. Error bars show SEM (n=13 dendrites in 13 cells from 13 animals).

(e) Amplitude nonlinearity corresponding to (d). The paired mean difference between near-synchronous (NS) and asynchronous separate responses (S) is 31% [95%CI 15%, 46%]. P= 0.004 (two-sided permutation t-test compared to 0%).

(f) uEPSP amplitude nonlinearity quantified by integral, plotted in the same way as (d).

(g) Integral nonlinearity corresponding to (f). The paired mean difference between near-synchronous (NS) and asynchronous separate responses (S) is 56% [95%CI 31%, 71%]. P<0.001 (two-sided permutation t-test compared to 0%).

Slopegraphs and Gardner-Altman estimation plots as in Fig. 2.

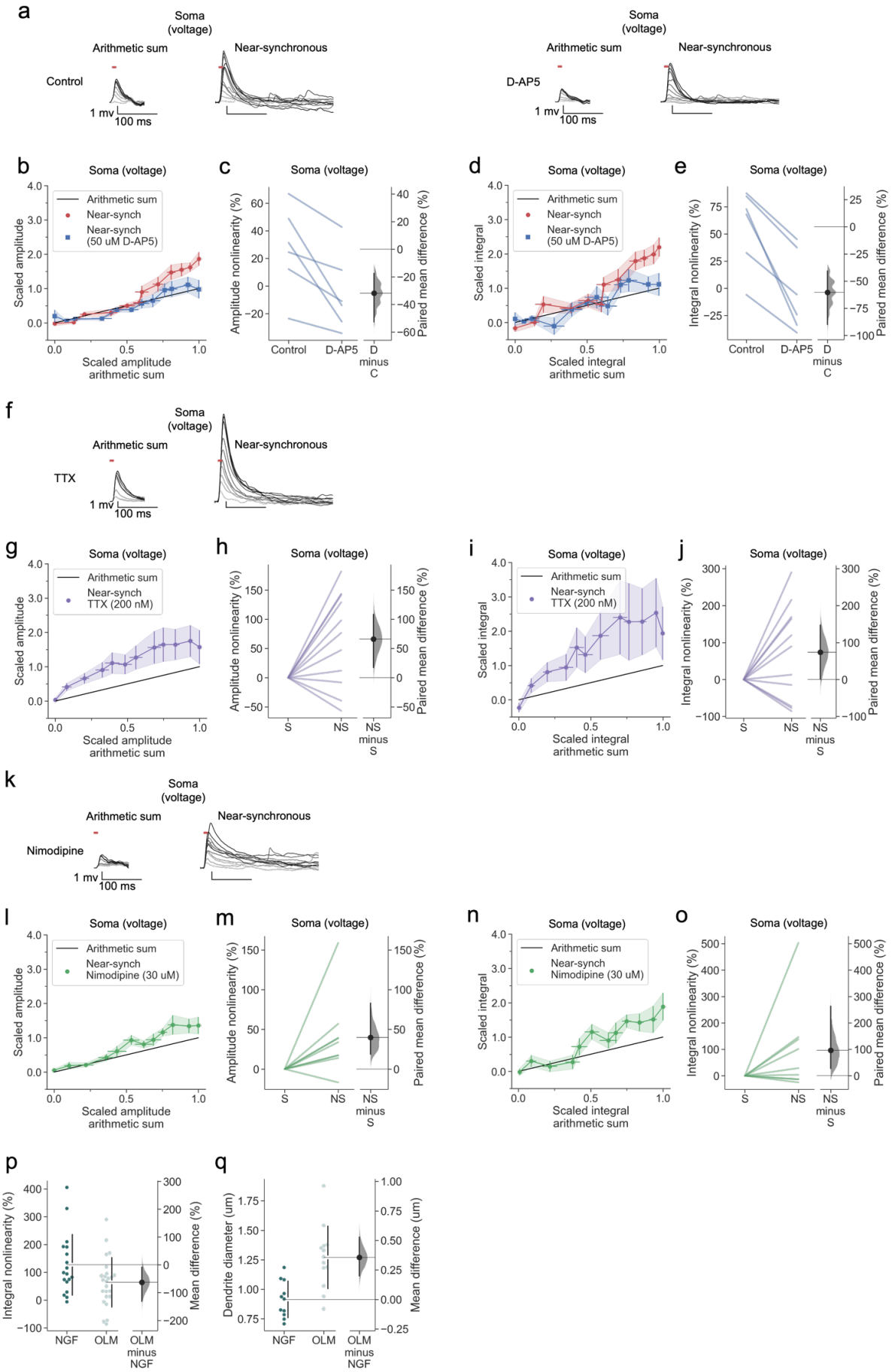
a
Soma (voltage)
Arithmetic sum
Near-synchronous
Control
D-AP5
1 mv
100 ms
b
c
d
e
Soma (voltage)
Arithmetic sum
Near-synch
Near-synch (50 uM D-AP5)
Scaled amplitude
Scaled amplitude arithmetic sum
Amplitude nonlinearity (%)
Paired mean difference (%)
Control
D-AP5
D minus C
Scaled integral
Scaled integral arithmetic sum
Integral nonlinearity (%)
f
TTX
g
h
i
j
Near-synch TTX (200 nM)
S
NS
NS minus S
k
Nimodipine
l
m
n
o
Near-synch Nimodipine (30 uM)
p
q
NGF
OLM
OLM minus NGF
Integral nonlinearity (%)
Mean difference (%)
Dendrite diameter (um)
Mean difference (um)

Fig. 8. Linear dendritic integration in neurogliaform interneurons with NMDARs blocked and no effect of voltage-dependent sodium channel nor of L-type voltage-dependent calcium channel blockade.

(a) Somatic uEPSPs evoked by uncaging glutamate in a representative neuron before (top) and after (bottom) D-AP5 (50 uM) perfusion. Uncaging protocol and data representation as in Figs. 1-2.

(b) Scaled amplitude of the recorded near-synchronous uEPSP plotted against scaled amplitude of the arithmetic sum, as the number of uncaging locations was increased. Error bars: SEM (n=6 dendrites in 6 cells from 6 animals).

(c) Amplitude nonlinearity for individual neurons shown in (b) before and after D-AP5 perfusion. The paired mean difference between the two conditions is -32% [95%CI -53%, -18%]. P<0.001 (two-sided permutation t-test).

(d) Scaled time-integral of uEPSPs plotted against scaled integral arithmetic sum of asynchronous separate responses, before and after NMDAR blockade.

(e) Integral nonlinearity corresponding to panel (d). The paired mean difference between baseline and D-AP5 conditions is -60% [95%CI -90%,-40%]. P <0.001 (two-sided permutation t-test).

(f) Somatic uEPSPs evoked by glutamate uncaging in one neuron in the presence of TTX (200 nM), showing supralinear uEPSP integration.

(g) Average scaled amplitude of the recorded near-synchronous uEPSP plotted against the arithmetic sum of the scaled asynchronous uEPSPs, as the cumulative number of uncaging locations was increased. Error bars: SEM (n=11 dendrites in 7 cells from 6 animals).

(h) Amplitude nonlinearity corresponding to (g). The paired mean difference between near-synchronous (NS) and asynchronous separate responses (S) is 66% [95%CI 17%, 102%]. P=0.029 (two-sided permutation t-test compared to 0%).

(i) uEPSP amplitude nonlinearity quantified by integral, plotted in the same way as (g).

(j) Integral nonlinearity corresponding to (i). The paired mean difference between near-synchronous (NS) and asynchronous separate responses (S) is 74% [95%CI 1%, 148%]. P=0.089 (two-sided permutation t-test compared to 0%).

(k) Somatic uEPSPs evoked by glutamate uncaging in one neuron in the presence of nimodipine (30 uM), showing supralinear uEPSP integration.

(l) uEPSP amplitude nonlinearity, plotted in the same way as (g). (n=8 dendrites in 7 cells from 7 animals).

(m) Amplitude nonlinearity corresponding to (l). The paired mean difference between near-synchronous (NS) and asynchronous separate responses (S) is 40% [95%CI 19%, 83%]. P=0.011 (two-sided permutation t-test compared to 0%).

(n) uEPSP amplitude nonlinearity quantified by integral, plotted in the same way as (g).

(o) Integral nonlinearity corresponding to (n). The paired mean difference between near-synchronous (NS) and asynchronous separate responses (S) is 97% [95%CI 27%, 263%]. P=0.066(two-sided permutation t-test compared to 0%).

(p) uEPSP amplitude nonlinearity quantified by integral in neurogliaform (NGF) and OLM interneurons (control and TTX experiments pooled). The mean difference between NGF and OLM integral nonlinearity is -63% [95%CI -132%, -8%]. P=0.0424 (two-sided permutation t-test).

(q) Dendritic diameter in NGF and OLM interneurons. The mean difference between NGF and OLM 0.36 [95%CI 0.20, 0.53]. P<0,001 (two-sided permutation t-test).

Slopegraphs and Gardner-Altman estimation plots as in Fig. 2.

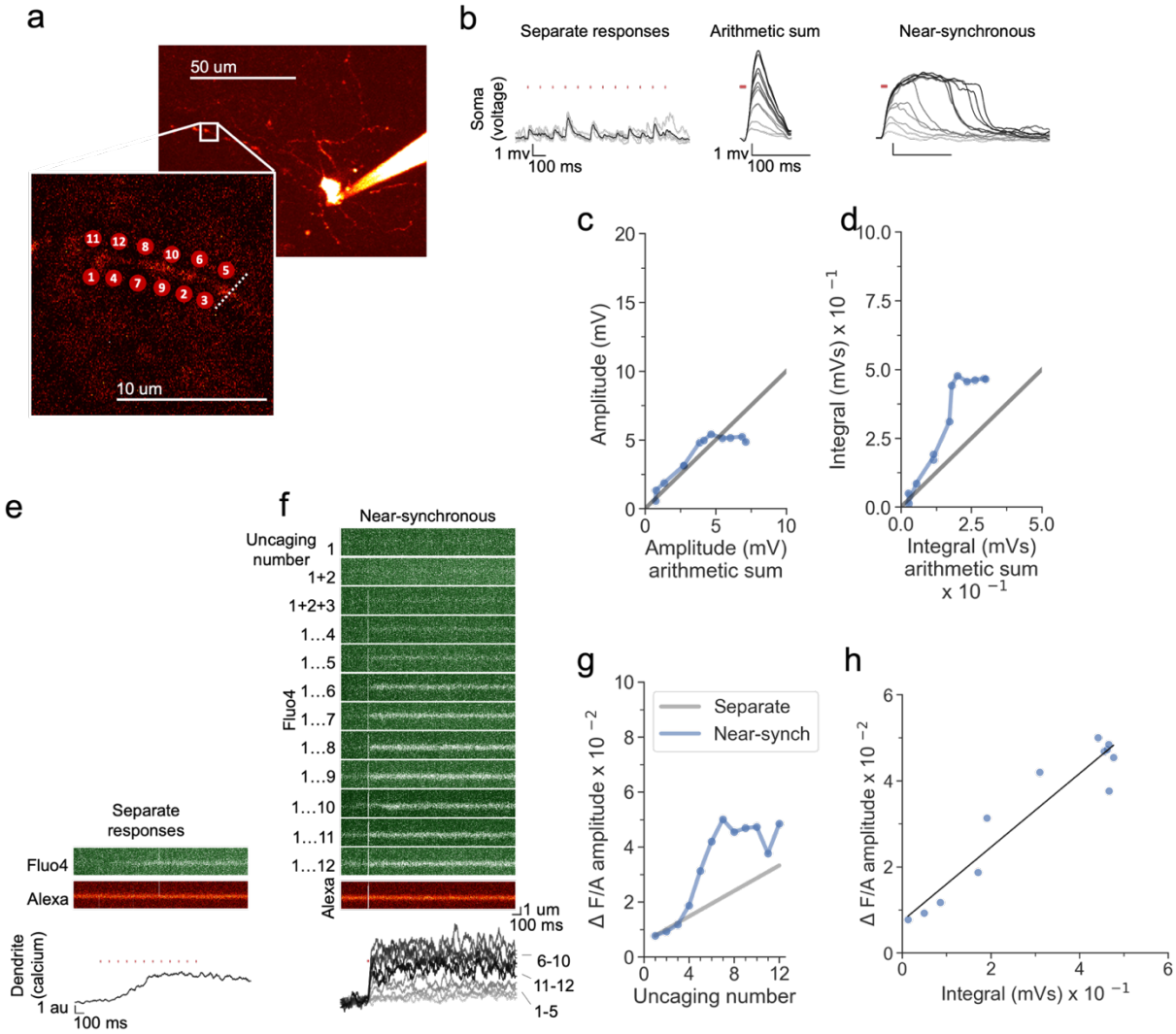
a
50 um
10 um
11
12
8
10
6
5
1
4
7
9
2
3
b
Separate responses
Arithmetic sum
Near-synchronous
Soma (voltage)
1 mv
100 ms
c
Amplitude (mV)
Amplitude (mV) arithmetic sum
d
Integral (mVs) x 10 −1
Integral (mVs) arithmetic sum x 10 −1
e
Separate responses
Fluo4
Alexa
Dendrite (calcium)
1 au
100 ms
f
Near-synchronous
Uncaging number
1
1+2
1+2+3
1…4
1…5
1…6
1…7
1…8
1…9
1…10
1…11
1…12
Fluo4
Alexa
1 um
100 ms
6-10
11-12
1-5
g
Separate
Near-synch
Δ F/A amplitude x 10 −2
Uncaging number
h
Δ F/A amplitude x 10 −2
Integral (mVs) x 10 −1

Supplementary Fig. S1. Comparison of uEPSP time-integral and dendritic calcium in a neurogliaform cell.

(a) Alexa-594 fluorescence Z-stack, with uncaging locations and linescan position (inset).

(b) Somatic voltage traces across asynchronous separate response and near-synchronous conditions, with times of uncaging stimuli indicated by red dots). In the asynchronous condition, individual traces are shown in grey, and the average shown in black. For the near-synchronous traces, light to dark traces indicate responses as the numbers of near-synchronous uncaging stimuli was increased from 1 to 12. The arithmetic sum traces are indicated in the same way.

(c) Peak amplitude of the recorded near-synchronous response plotted against the amplitude of the arithmetic sum for increasing numbers of uncaging locations.

(d) Integralof the recorded near-synchronous response plotted against the integral of the arithmetic sum.

(e) Fluo-4 linescans in response to asynchronous stimulation. Locations 1 – 12 were sequentially stimulated at times indicated by red dots.

(f) Fluo-4 linescan in response to near-synchronous stimulation of increasing numbers of locations. The Fluo-4 fluorescence change from baseline was normalised to the fluorescence of the inert morphological dye Alexa-594 (the average linescan for Alexa-594 is shown beneath). Laser uncaging stimuli are indicated by red dots above the traces. Ratiometric calcium traces use arbitrary units (au).

(g) Fluo-4 fluorescence transient amplitude, normalised by Alexa-594 fluorescence, showing a deviation from the predicted response to asynchronous stimulation when more than 4 locations were uncaged near-synchronously. Grey line indicates the estimated asynchronous response amplitude using interpolated values (see methods).

(h) Fluo-4 fluorescence transient (normalised to Alexa-594 fluorescence) plotted against uEPSP integral.

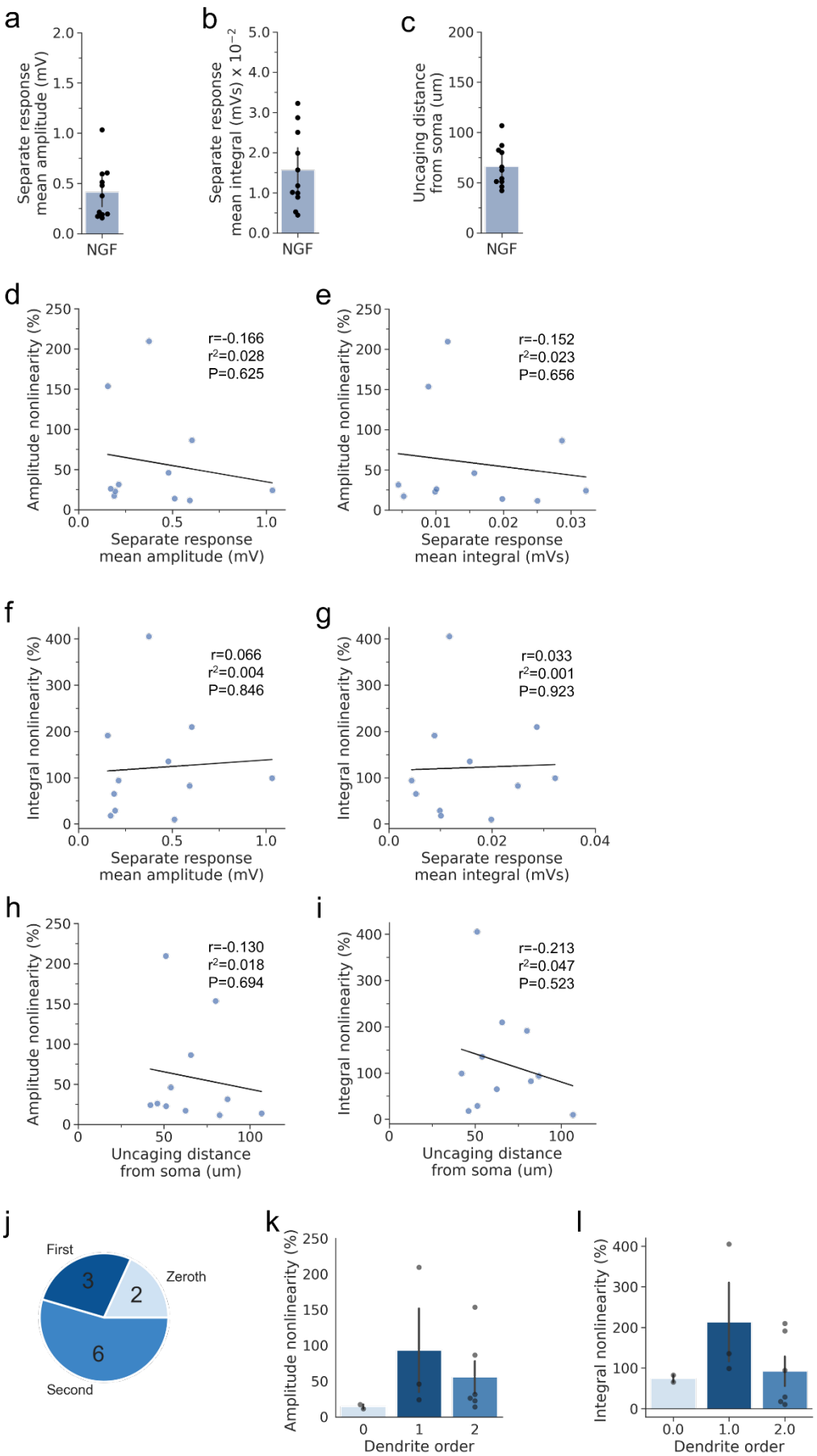
a
Separate response mean amplitude (mV)
NGF
b
Separate response mean integral (mVs) x 10−2
NGF
c
Uncaging distance from soma (um)
NGF
d
Amplitude nonlinearity (%)
r=-0.166
r2=0.028
P=0.625
Separate response mean amplitude (mV)
e
Amplitude nonlinearity (%)
r=-0.152
r2=0.023
P=0.656
Separate response mean integral (mVs)
f
Integral nonlinearity (%)
r=0.066
r2=0.004
P=0.846
Separate response mean amplitude (mV)
g
Integral nonlinearity (%)
r=0.033
r2=0.001
P=0.923
Separate response mean integral (mVs)
h
Amplitude nonlinearity (%)
r=-0.130
r2=0.018
P=0.694
Uncaging distance from soma (um)
i
Integral nonlinearity (%)
r=-0.213
r2=0.047
P=0.523
Uncaging distance from soma (um)
j
First
Zeroth
Second
3
2
6
k
Amplitude nonlinearity (%)
Dendrite order
l
Integral nonlinearity (%)
Dendrite order

Supplementary Fig. S2. Relationships among uncaging parameters and uEPSP nonlinearity (NGF).

(a) Mean asynchronous separate response uEPSP amplitude.

(b) Mean asynchronous separate response uEPSP integral.

(c) Distance from the soma to the uncaging location along the dendrite.

(d) Separate response mean amplitude plotted against amplitude nonlinearity following near-synchronous uncaging.

(e) Separate response mean integral plotted against amplitude nonlinearity following near-synchronous uncaging.

(f) Separate response mean amplitude plotted against integral nonlinearity following near-synchronous uncaging.

(g) Separate response mean integral plotted against integral nonlinearity following near-synchronous uncaging.

(h) Uncaging distance from soma plotted against amplitude nonlinearity.

(i) Uncaging distance from soma plotted against integral nonlinearity.

(j) Dendritic order for dendrites used for glutamate uncaging. The numbers in the pie chart represent the numbers of dendrites in the respective categories.

(k) Amplitude nonlinearity split by dendrite order.

(l) integral nonlinearity split by dendrite order.

Linear regressions are depicted as black lines. Pearson correlation parameters depicted in correlation panels. Summary values are depicted as mean ± SEM. n=11 dendrites in 11 cells from 9 animals.

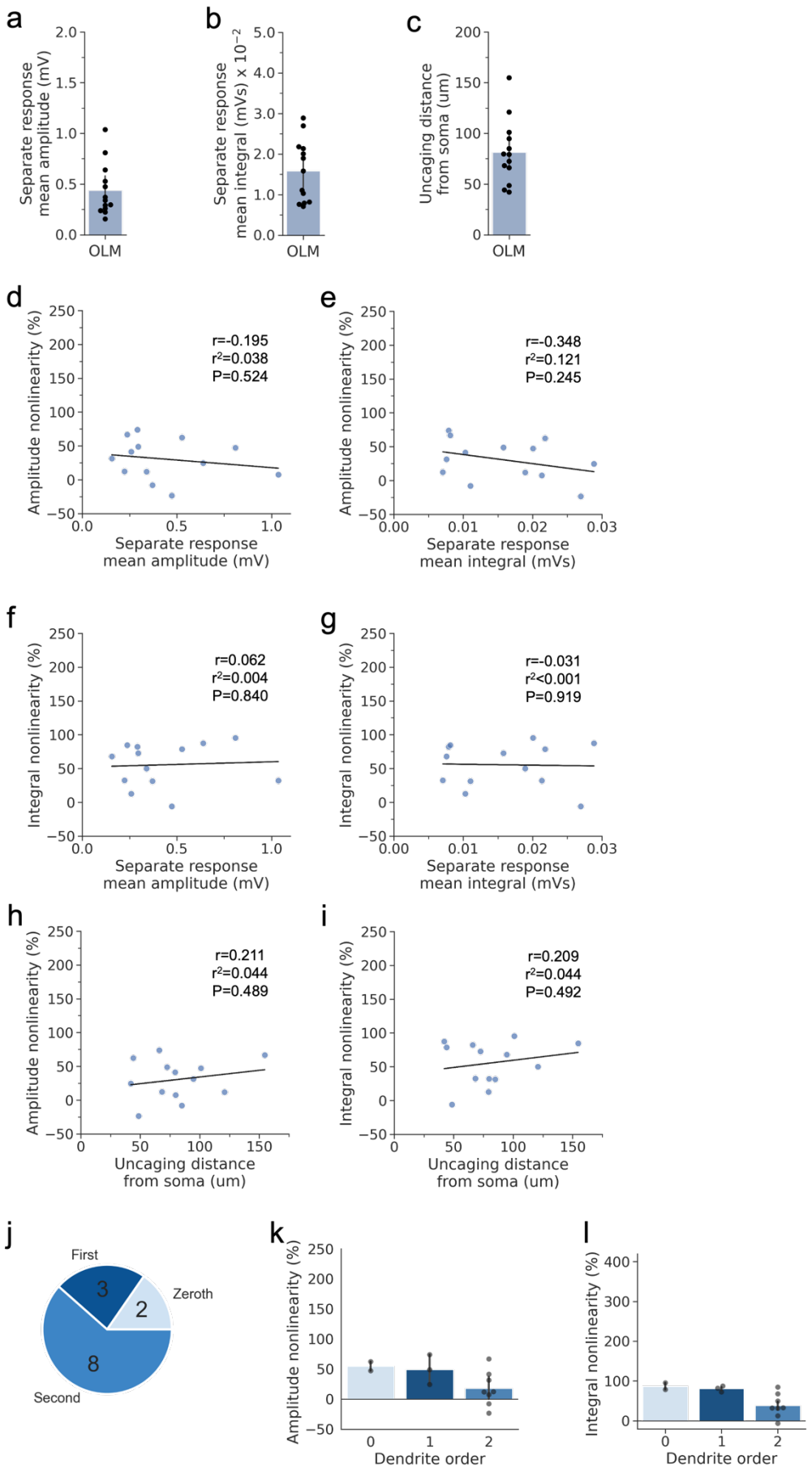
a
Separate response mean amplitude (mV)
OLM
b
Separate response mean integral (mVs) x 10⁻²
OLM
c
Uncaging distance from soma (um)
OLM
d
Amplitude nonlinearity (%)
r=-0.195
r²=0.038
P=0.524
Separate response mean amplitude (mV)
e
Amplitude nonlinearity (%)
r=-0.348
r²=0.121
P=0.245
Separate response mean integral (mVs)
f
Integral nonlinearity (%)
r=0.062
r²=0.004
P=0.840
Separate response mean amplitude (mV)
g
Integral nonlinearity (%)
r=-0.031
r²<0.001
P=0.919
Separate response mean integral (mVs)
h
Amplitude nonlinearity (%)
r=0.211
r²=0.044
P=0.489
Uncaging distance from soma (um)
i
Integral nonlinearity (%)
r=0.209
r²=0.044
P=0.492
Uncaging distance from soma (um)
j
First
Zeroth
Second
3
2
8
k
Amplitude nonlinearity (%)
Dendrite order
l
Integral nonlinearity (%)
Dendrite order

Supplementary Fig. S3. Relationships among uncaging parameters and uEPSP nonlinearity (OLM).

(a) Mean asynchronous separate response uEPSP amplitude.

(b) Mean asynchronous separate response uEPSP integral.

(c) Distance from the soma to the uncaging location along the dendrite.

(d) Separate response mean amplitude plotted against amplitude nonlinearity following near-synchronous uncaging.

(e) Separate response mean integral plotted against amplitude nonlinearity following near-synchronous uncaging.

(f) Separate response mean amplitude plotted against integral nonlinearity following near-synchronous uncaging.

(g) Separate response mean integral plotted against integral nonlinearity following near-synchronous uncaging.

(h) Uncaging distance from soma plotted against amplitude nonlinearity.

(i) Uncaging distance from soma plotted against integral nonlinearity.

(j) Dendritic order for dendrites used for glutamate uncaging. The numbers in the pie chart represent the numbers of dendrites in the respective categories.

(k) Amplitude nonlinearity split by dendrite order.

(l) integral nonlinearity split by dendrite order.

Linear regressions are depicted as black lines. Pearson correlation parameters depicted in correlation panels. Summary values are depicted as mean ± SEM. N= 13 dendrites, in 13 cells, from 13 animals.

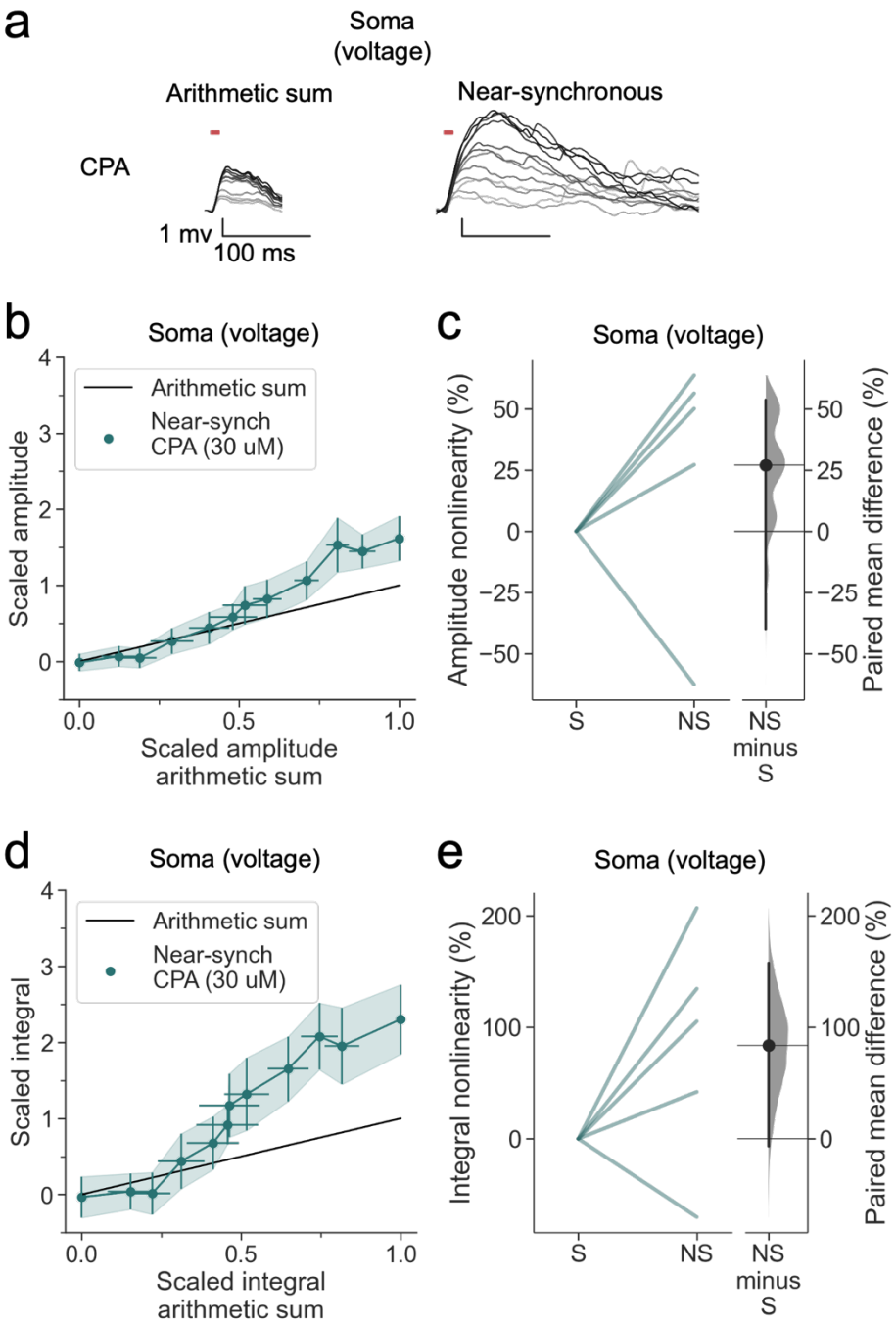
a
Soma
(voltage)
Arithmetic sum
Near-synchronous
CPA
1 mv
100 ms
b
Soma (voltage)
Arithmetic sum
Near-synch
CPA (30 uM)
Scaled amplitude
Scaled amplitude
arithmetic sum
c
Soma (voltage)
Amplitude nonlinearity (%)
Paired mean difference (%)
S
NS
NS
minus
S
d
Soma (voltage)
Arithmetic sum
Near-synch
CPA (30 uM)
Scaled integral
Scaled integral
arithmetic sum
e
Soma (voltage)
Integral nonlinearity (%)
Paired mean difference (%)
S
NS
NS
minus
S

Supplementary Fig. S4. SERCA inhibition does not affect supralinear dendritic summation in OLM interneurons.

(a) Somatic uEPSPs evoked by glutamate uncaging in one neuron in the presence of CPA (30 uM), showing supralinear uEPSP integration.

(b) Average scaled amplitude of the recorded near-synchronous uEPSP plotted against the arithmetic sum of the scaled asynchronous uEPSPs, as the cumulative number of uncaging locations was increased. Error bars show SEM (n=5 dendrites in 4 cells from 4 animals).

(c) Amplitude nonlinearity corresponding to (b). The paired mean difference between near-synchronous (NS) and asynchronous separate responses (S) is 27% [95%CI -40%, 54%]. P= 0.239 (two-sided permutation t-test compared to 0%).

(d) uEPSP amplitude nonlinearity quantified by integral, plotted in the same way as (b).

(e) Integral nonlinearity corresponding to (g). The paired mean difference between near-synchronous (NS) and asynchronous separate responses (S) is 84% [95%CI -7%, 158%]. P=0.123 (two-sided permutation t-test compared to 0%).

Slopegraphs and Gardner-Altman estimation plots as in Fig. 2